Dyes and Pigments 216 (2023) 111361

Contents lists available at ScienceDirect

Dyes and Pigments

journal homepage: www.elsevier.com/locate/dyepig

Comparative (magneto)optical, redox, and photophysical properties of phosphorous octacarbazole- and tetra-*tert*-butyltetrabenzotriazacorroles

Basma Ghazal [a], Dustin E. Nevonen [b,c], Lubna Salah [d], Ali Shuaib [e], Victor N. Nemykin [b,*], Saad Makhseed [d,**]

[a] Department of Organometallic and Organometalloid Chemistry Division, National Research Centre, Giza, Egypt
[b] Department of Chemistry, University of Tennessee, Knoxville, TN, 37996, USA
[c] Department of Chemistry, University of Manitoba, Winnipeg, MB, Canada
[d] Department of Chemistry, Kuwait University, P.O. Box 5969, Safat, 13060, Kuwait
[e] Biomedical Engineering Unit, Department of Physiology, Faculty of Medicine, Kuwait University, P.O. Box 24923, Safat, 13110, Kuwait

A B S T R A C T

The spectroscopy and electronic structure of the novel phosphorous(V) octacarbazole tetrabenzotriazacorrole (**TBC$^{(Cz)8}$P=O**) compound were evaluated using a large array of experimental and theoretical methods, and compared to the reference terta-*tert*-butyl tetrabenzotriaazacorrole (**TBC$^{(tBu)4}$P=O**). The first coordination sphere in **TBC$^{(Cz)8}$P(XY)** and **TBC$^{(tBu)4}$P(XY)** in a solid state and solution was probed by MALDI-TOF mass spectrometry, ^{31}P NMR spectroscopy, XPS, UV–Vis, MCD, and elemental analysis. Based on the ^{31}P NMR, mass spectrometry, UV–Vis, and MCD data, it was demonstrated that the initial pentacoordinated **TBC$^{(tBu)4}$P=O** complex can be easily transformed to the hexa-coordinated species in the presence of water and methanol following **TBC$^{(tBu)4}$P=O** ⇌ **TBC$^{(tBu)4}$P(OH)$_2$** ⇌ **TBC$^{(tBu)4}$P(OH)(OMe)** ⇌ **TBC$^{(tBu)4}$P(OMe)$_2$** equilibrium. In wet solvents, the UV–Vis and MCD spectroscopies revealed that the two structures possess similar absorbance profiles; however, the **TBC$^{(Cz)8}$P(OH)$_2$** compound had a more intense and red-shifted *Q*-band than the **TBC$^{(tBu)4}$P(OH)$_2$** compound. The first oxidation under spectroelectrochemical conditions was found to be completely reversible for the **TBC$^{(Cz)8}$P(OH)$_2$** compound; conversely, these experiments were completely irreversible for the **TBC$^{(tBu)4}$P(OH)$_2$** compound. DFT and TDDFT calculations were performed using three different exchange-correlation functionals. The DFT results revealed several (16 in total) carbazole-centered MOs at energies in between the classical Gouterman's a_{1u} and a_{2u} frontier orbitals while the four Gouterman's frontier orbitals were found to be energetically sequential for the **TBC$^{(tBu)4}$P(OH)$_2$** compound. The TDDFT calculations provided a very reasonable agreement between theory and experiment and demonstrated the presence of the inter-ligand (carbazole-to-TBC) charge-transfer transitions in **TBC$^{(Cz)8}$P(OH)$_2$** in ~500 nm region. Steady-state fluorescence spectroscopy data are indicative of the mid-range fluorescence quantum yields in both compounds. Transient absorption spectroscopy was utilized to probe triplet state formation and lifetimes (τ_T) which were found to be 112 μs for **TBC$^{(Cz)8}$P(OH)$_2$** and 91 μs for **TBC$^{(tBu)4}$P(OH)$_2$**.

1. Introduction

The corrole ring (**Corr**, Fig. 1) is comprised of four nitrogen atoms within its macrocyclic core and a total of 19 carbon atoms in the molecule [1–8]. When compared to porphyrins (Fig. 1), corroles possess attractive properties such as higher fluorescence quantum yields, intense absorption in the red region of the optical region, redox non-innocence and lower first oxidation potentials, as well as more significant Stokes shifts. Corroles are trianionic planar ligands that can stabilize the higher oxidation states of different main-group and transition-metal ions, which make corroles a suitable material for many different applications including catalysis, artificial photosynthesis, and biomedical applications [9–25]. By attaching various metals to the corrole macrocycle, one can tune the optical properties by changing the energy gaps of the frontier molecular orbitals, which can then be used for biomedical imaging and sensing [26–28]. In contrast, despite their discovery by Gouterman's group in 1981 [29], until recently introduced by Goldberg's group [30–36], triazacorroles (**TAC**, also known as corrolazines) and tetrabenzotriazacorroles (**TBC**, Fig. 1) were limited to their phosphorous, silicon, tin, aluminum, and germanium derivatives [37–43]. Main-group **TBC** derivatives are known to have a slightly blue-shifted (compared to phthalocyanines) *Q*-band of lower intensity and a very characteristic intense transition in the 400–450 nm region [44–50]. More importantly, phosphorous **TBCs** were found to form triplet states and to be effective photosensitizers for singlet oxygen production which is useful for photodynamic therapy (PDT) of cancer application [51–53]. Despite significant progress in the chemistry of **TBCs**, when bio-applications are considered, these platforms still suffer

* Corresponding author.
** Corresponding author.
E-mail addresses: vnemykin@utk.edu (V.N. Nemykin), saad.makhseed@ku.edu.kw (S. Makhseed).

https://doi.org/10.1016/j.dyepig.2023.111361
Received 15 February 2023; Received in revised form 26 April 2023; Accepted 27 April 2023
Available online 6 May 2023

from the typical (for phthalocyanines) aggregation problems and blue-shifted (compared to phthalocyanines) position of their *Q*-band. We have recently shown that because of a bulky nature of carbazole groups, octa-carbazole substituted phthalocyanine and respective transition-metal complexes remain monomeric in a large range of concentrations. In addition, their *Q*-bands are red-shifted compared to those of typical phthalocyanines [54,55]. In this work, we introduce phosphorus octacarbazoltetrabenzotriazacorrole (**TBC$^{(Cz)8}$P=O**) and compare its photophysical properties with the reference tetra-*tert*-butyltetrabenzotriazacorrole (**TBC$^{(tBu)4}$P=O**, Scheme 1).

2. Results and discussion

2.1. Synthesis

The reference tetra-*tert*-butyltetrabenzotriazacorrole (**TBC$^{(tBu)4}$P=O**) (Scheme 1) was reported by Hanack and co-workers [56], by Tomilova and co-workers [57] and later on by Giribabu and co-workers [48]. Its synthesis follows a procedure established by Gouterman in 1981 [29]. There is some controversy present for the structure of unsubstituted and alkyl-substituted phosphorous **TBCs**. The controversial nature of phosphorus **TBCs** is derived from the attributes of the axially coordinated phosphorus which is bound either to an oxygen atom through a double-bond (penta-coordinated **TBC^{Rn}P=O** compound) or to two axial groups (hexa-coordinated **TBC^{Rn}P(OR)$_2$** structures with R = H or Me, respectively) [48,50,56–58]. In addition, a third, salt-like structure, **[TBCP(OH)]$^+$(OH)$^-$** was also proposed by Goldberg and co-authors for α-octabutoxy-substituted TBCs [58]. It is commonly accepted that the combination of ^{31}P NMR spectroscopy and mass spectrometry can provide an ultimate knowledge on the first coordination sphere of phosphorous **TBCs**. In several cases, XPS, IR, and X-ray crystallographic data were used to solidify the conclusions. It is well-known that six-coordinated phosphorous porphyrin, corrole, phthalocyanine, tetraazacorroles, and **TBCs** have signals in the −180 to −200 ppm region of their ^{31}P NMR spectra (Table 1) [58]. Contrarily, penta-coordinated systems of the same macrocycles have ^{31}P NMR signals in the −90 to −110 ppm region and these data correlate well with the available X-ray crystallographic data (Table 1). As we will show below, the general trends in the axial coordination of phosphorous(V) **TBCs** follows that established for corrole analogues [59–73].

In case of the unsubstituted phosphorous(V) **TBC** in a very accurate study, Bender and co-workers showed that the electronic ionization TOF mass spectrum of this compound obtained by double sublimation in vacuum has only a molecular ion that corresponds to the penta-coordinated **TBCP=O** compound [50]. The XPS analysis of the vacuum deposited (sublimed) film as well as elemental analysis of the sample dried overnight under vacuum are also consistent with this formula; however, its ^{31}P NMR spectrum in a Py/$CDCl_3$ (10:90% v/v) mixture has a single signal at −202.0 ppm, which is characteristic for the hexa-coordinated phosphorous(V) species (Table 1). Similarly, Hanack and co-workers [56] observed (using the FAB mass spectrometry method) penta-coordinated **TBC$^{(tBu)4}$P=O** and **TBC$^{(β-C5H11)8}$P=O** molecular ions, while the ^{31}P NMR spectra of these compounds in $CDCl_3$ have peaks at −186.7 and −189.4 ppm, respectively. Moreover, these authors mentioned that "besides the main signal, a second minor signal close to the main one is also observed, indicating that a different coordination environment for P^V may exist." Tomilova and co-authors [57] also reported that **TBC$^{(tBu)4}$P=O** and **TBC$^{(β-C4H9)8}$P=O** compounds have molecular ions in their MALDI-TOF spectra that correspond to the penta-coordinated species, while their ^{31}P NMR spectra in a Py/$CDCl_3$ (1:1 v:v) mixture has signals observed at −201.7 ppm, which correspond to the hexa-coordinated species. Furthermore, in $CDCl_3$, these authors observed two peaks for the **TBC$^{(β-C4H9)8}$P=O** molecule: one at −201 and another at −105 ppm with the latter one being characteristic to the penta-coordinated species. In order to clarify such controversy, we have prepared two samples of **TBC$^{(tBu)4}$P(XY)**, which differ by the purification protocols. The first sample was chromatographed using DCM (100-95%)/MeOH(0–5%) gradient. Pure fraction of this sample then was evaporated to dryness using a standard rotary evaporator at 50 °C for several minutes. When dissolved in $CDCl_3$, this sample gives two signals in its ^{31}P NMR spectrum (Supporting Information Fig. S1a). The main signal at −187.9 ppm correlate well with that reported by Hanack

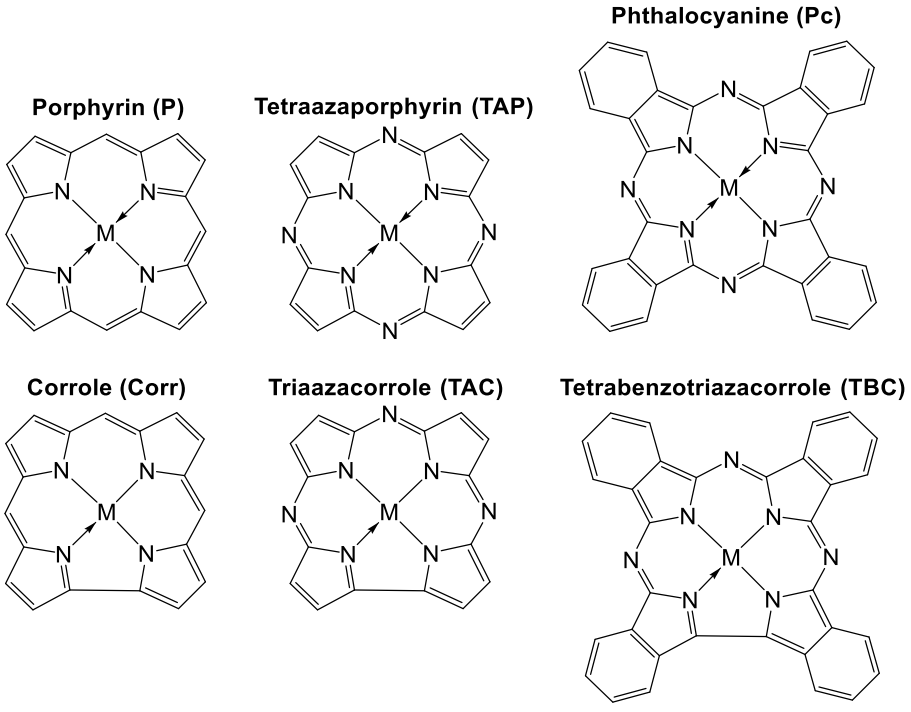

Fig. 1. Comparison between the structures of unsubstituted porphyrin and corrole, tetraazaporphyrin and triazacorrole, and phthalocyanine and tetrabenzotriazacorrole.

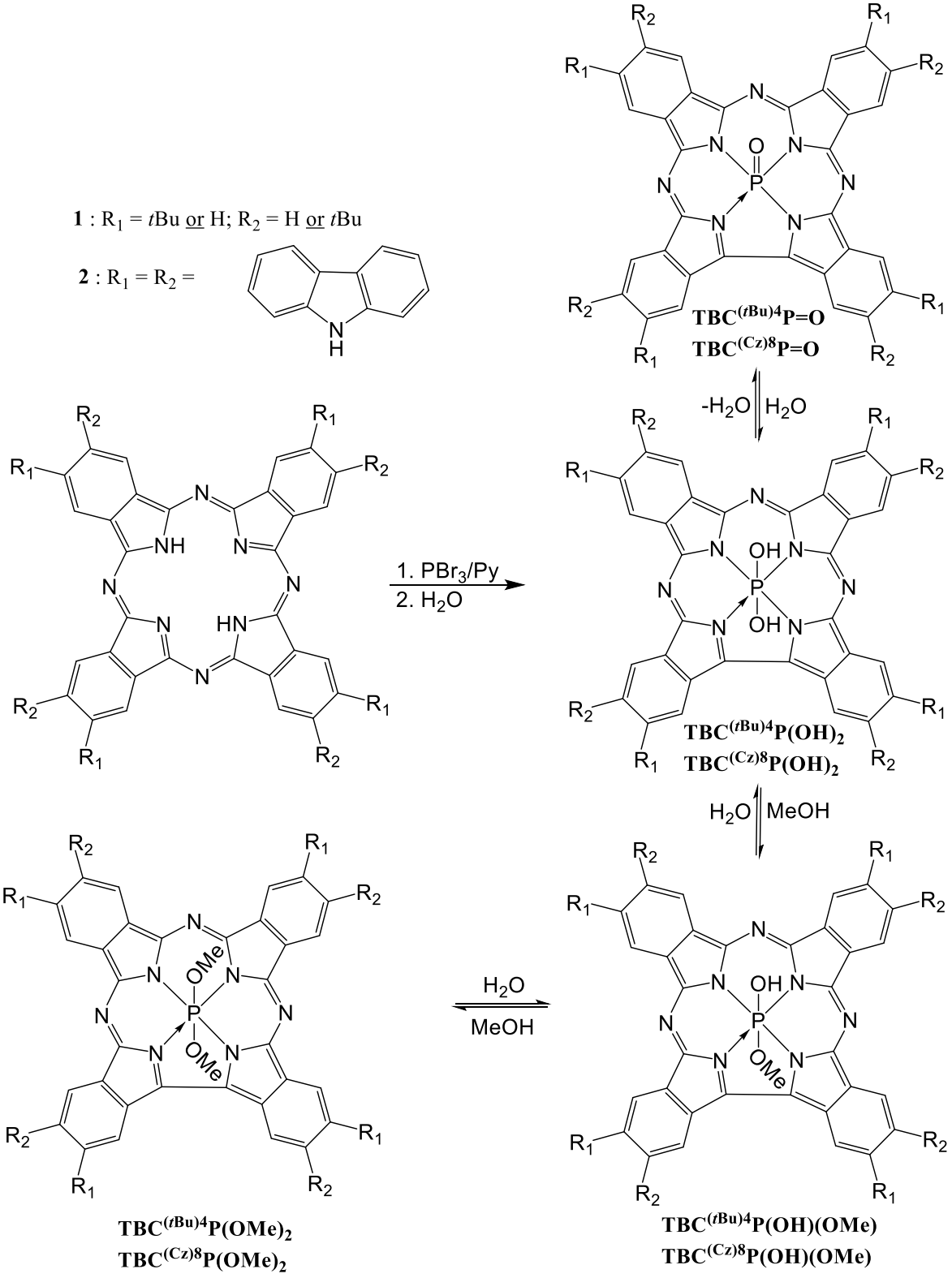

Scheme 1. Synthesis of **TBC$^{(Cz)8}$P(XY)** and **TBC$^{(tBu)4}$P(XY)** complexes.

and co-workers in the same solvent [56]. The presence of the minor signal observed at −194.8 ppm was also mentioned (but not interpreted) by the same group. Both signals are indicative of the presence of hexa-coordinated **TBCs**. When the same sample was dissolved in pyridine-d5, we observed only one signal at −200.9 ppm (Supporting Information Fig. S1b). This signal correlates well with data from Bender and co-workers for unsubstituted **TBC** [50] dissolved in pyridine as well as Tomilova and co-workers for alkyl-substituted **TBCs** [57] dissolved in Py/$CDCl_3$ (1:1 v/v) mixture (Table 1).

The second sample was obtained without use of methanol and dried in vacuum oven at 100 °C for several hours. When this sample was dissolved in dry $CDCl_3$ (400 μL) in vacuum-dried NMR tube, the only

Table 1
^{31}P NMR and other selected data for selected phosphorous(V) triazacorroles, corroles, phthalocyanines, and porphyrins.

Compound	CN[a]	^{31}P NMR (solv.)	X-ray	MS[b]	ref
Tetrabenzotriazacorroles					
TBC$^{(Cz)8}$P(OH)$_2$	6	−198.5 Py	no	MALDI	tw
TBC$^{(tBu)4}$P(OH)$_2$	6	−200.9 Py	no	MALDI	tw
TBC$^{(tBu)4}$P(OH)$_2$	6	−202.5 $CDCl_3$/	no	MALDI	tw
TBC$^{(tBu)4}$P(OH)(OMe)	6	Py (98:2 v/v)[c]	no	MALDI	tw
TBC$^{(tBu)4}$P(OMe)$_2$	6	−194.9[d] $CDCl_3$	no	MALDI	tw
TBC$^{(tBu)4}$P=O	5	−187.9[e] $CDCl_3$ −106.3 $CDCl_3$ (dry)	no	MALDI	tw
TBC$^{(tBu)4}$P=O ?[f]	5?	−201.7 Py/ $CDCl_3$ 1:1	no	MALDI	57
TBC$^{(tBu)4}$P=O ?[g]	5?	−186.7 $CDCl_3$	no	FAB	56
TBC$^{(C4H9)8}$P=O ?[f]	5?	−201.7 Py/ $CDCl_3$ 1:1	no	MALDI	57
TBC$^{(C4H9)8}$P=O ?[h]		−201 (−105) $CDCl_3$			57
TBC$^{(nC5H11)8}$P=O ?[g]	5?	−189.4 $CDCl_3$	no	FAB	56
TBC$^{(iPrO)4}$P(OH)$_2$	6	−202.8 DMSO	no	MALDI	64
TBC$^{(α-PhO)4}$P(OH)$_2$	6	−201.3 Py	no	MALDI [M − H_2O]	65
TBC$^{(β-PhO)4}$P(OH)$_2$	6	−201.3 Py	no	MALDI [M − H_2O]	65
TBCP(Ph)$_2$	6	−212.0 Py	no	MALDI [M-Ph]$^+$	66
TBCP(C_8H_{17})$_2$	6	−208.2 Py	no	MALDI [M − C_8H_{17}]$^+$	66
TBC$^{(α-BuO)8}$P(OCH$_3$)$_2$	6	−186.1 $CDCl_3$	no	MALDI	58
[TBC$^{(α-BuO)8}$P(OH)]$^+$OH$^-$	5	−105.1 $CDCl_3$	no	MALDI [M + OH]$^+$	58
[TBC$^{(α-BuO)8Cl8}$P(OH)]$^+$OH$^-$	5	−105.1 $CDCl_3$	no	MALDI [M + OH]$^+$	58
TBCP=O ?[g]	5?	−202.0 Py/ $CDCl_3$ 9:1	no	EI	50
TBCP(OH)$_2$	6	−200.7 Py	no	MALDI	67
TBC$^{(SO3H)n}$P(OH)$_2$	6	−201.5 DMSO	no	MALDI	68
TBC$^{(SO3H)4}$P(OH)$_2$	6	−201.5 DMSO	no	MALDI	67
TBC$^{(PhO)8}$P(OSiPh$_3$)$_2$	6	−216 Py	yes	MALDI	69
TBC$^{(PhO)8}$P(OH)$_2$	6	−200 Py	no	MALDI	69
[TBC$^{(tBuPhO)8}$P(OH)]$^+$OH$^-$	5	−106.3 $CDCl_3$	no	MALDI-OH	70
Phthalocyanines					
[*Pc*$^{(tBu)4}$P(OH)$_2$]$^+$OH$^-$	6	−189 Py/$CDCl_3$ 1:1	no	MALDI	57
[*Pc*$^{(tBu)4}$P(OH)$_2$]$^+$OH$^-$	6	−166.0 $CDCl_3$	no	FAB [M − OH]$^+$	56
[*Pc*$^{(Pr)8}$P(OH)$_2$]$^+$OH$^-$	6	−164.0 $CDCl_3$	no	FAB [M − OH]$^+$	56
[*Pc*$^{(Bu)8}$P(OH)$_2$]$^+$OH$^-$	6	−201 Py:$CDCl_3$ 1:1	no	MALDI	57
[*Pc*$^{(α-BuO)8}$P(OCH$_3$)$_2$]$^+$OH$^-$	6	−179.8 $CDCl_3$	no	MALDI	58
Triazacorrolazines					
[TAC$^{(TBP)8}$P(OH)]$^+$OH$^-$	5	−111.2 $CDCl_3$	no	FAB	33
TAC$^{(TBP)8}$P(OCH$_3$)$_2$	6	−192.1C_6D_6	yes	MALDI	33
[TAC$^{(MeOP)8}$P(OH)]$^+$OH$^-$	5	−111.4 $CDCl_3$	no	LD[M − OH]$^+$	35
TAC$^{(MeOP)8}$P(OCH$_3$)$_2$	6	−192.7C_6D_6	yes	LD[M-Ome]$^+$	35
Corroles					
(OEC)P=O	6	−99.40 $CDCl_3$	no	EI	71
[(EMC)P(OH)]$^+$Cl$^-$	5	−102.5 ?	yes	EI	72
Corr$^{(Ph)3}$P=O	5	−100.7	no	na	59
Corr$^{(Ph)3}$P(OH)$_2$	6	−191.5	no	"Q-TOF"	59
Corr$^{(Ph)3}$P(OH(OMe)	6	−184.1	no	na	59
Corr$^{(Ph)3}$P(OMe)$_2$	6	−176.8	yes	na	59
Porphyrins					
[OEPP(CH_2CH_3)(OH)]$^+$$ClO_4^-$	6	−179.8 $CDCl_3$	yes	na	68
[OEPP(C_6H_5)($OCH_2CH_2CH_3$)]$^+$$ClO_4^-$	6	−186.7 $CDCl_3$	yes	na	68
[OEPP(OH)$_2$]$^+$$ClO_4^-$	6	−183 (−191) acetone	no	na	29
[mesoDMEP(OH)$_2$]$^+$$PF_6^-$	6	−190 acetone	no	na	29
[mesoDMEP(OH)$_2$]$^+$$PF_6^-$	6	(-192) −193 MeOH	no	na	29

[a] CN = coordination number.
[b] Mass spectrum. [M]$^+$ ions were detected, otherwise peaks are mentioned next to the method used.
[c] Same peak observed in $CDCl_3$/D_2O (99.5:0.5 v/v) solution.
[d] Minor peak for sample 1. For this peak appearance in $CDCl_3$/MeOH-d4 system, see ^{31}P spectra in supporting information.
[e] Major peak for sample 1. For this peak appearance in $CDCl_3$/MeOH-d4 system, see ^{31}P spectra in supporting information.
[f] Highly likely **TBC$^{(tBu)4}$P(OH)$_2$** complex;[g] Highly likely **TBC$^{(tBu)4}$P(OMe)$_2$** complex.
[h] Highly likely that the major signal at −201 ppm belongs to **TBC$^{(C4H9)8}$P(OH)$_2$** complex and the minor signal at −105 ppm belongs to **TBC$^{(C4H9)8}$P=O** complex.

signal was observed at −106.3 ppm (Supporting Information Fig. S2). This signal is indicative of penta-coordinated **TBC$^{(tBu)4}$P=O** complex. Adding of just 2 μL of D_2O to this solution leads to disappearance of this peak and appearance of a new peak at −202.5 ppm (Supporting Information Fig. S2). This peak is reflective of hexa-coordinated complex. Similarly, addition of 1 and 7 μL of wet pyridine-d5 to solution of **TBC$^{(tBu)4}$P=O** complex in dry $CDCl_3$ results in gradual increase of signal at −202.5 ppm and decrease of signal at −106.3 ppm (Supporting Information Fig. S4). The position of −202.5 ppm signal in both cases correlate well with the −200.9 ppm signal obtained in pure pyridine-d5 for sample 1 discussed above. Thus, we conclude that the residual water in any organic solvent can easily hydrate **TBC$^{(tBu)4}$P=O** complex with the formation of hexa-coordinated **TBC$^{(tBu)4}$P(OH)$_2$** compound (Scheme 1). Initial addition of 1 μL of wet methanol-d4 to a solution of **TBC$^{(tBu)4}$P=O** complex in dry $CDCl_3$ results in the appearance of two signals at −187.9 and −194.9 ppm (Supporting Information Fig. S3). Further addition of methanol-d4 leads to increase of the intensity of −187.9 ppm signal and decrease of signal at −194.9 ppm. The final spectrum resembles that of sample 1 in $CDCl_3$. Based on the titration experiments, we assign the −187.9 ppm signal to **TBC$^{(tBu)4}$P(OMe)$_2$** complex and the signal at −194.9 ppm to **TBC$^{(tBu)4}$P(OH)(OMe)** complex. Thus each of stepwise substitution of the axial OH^- group to MeO^- in **TBC$^{(tBu)4}$P(OH)$_2$** leads to ~7 ppm downfield shift. The same ~7 ppm shift was observed by Ravikanth and co-workers in **Corr$^{(Ph)3}$P=O** ⇌ **Corr$^{(Ph)3}$P(OH)$_2$** ⇌ **Corr$^{(Ph)3}$P(OH)(OMe)** ⇌ **Corr$^{(Ph)3}$P(OMe)$_2$** transformation of phosphorous(V) corrole upon titration with methanol [59].

Similar to NMR experiments, we have conducted a number of MALDI investigations. Deposition of the **TBC$^{(tBu)4}$P(OMe)$_2$** sample 1 (obtained in the presence of methanol) onto a MALDI plate surface using regular (wet) DCM results in the spectrum shown in Fig. 2A. Four peaks can be easily identified in the spectrum. These belong to **[TBC$^{(tBu)4}$P]$^+$**, **[TBC$^{(tBu)4}$P=O]$^+$**, **[TBC$^{(tBu)4}$P(OH)$_2$]$^+$**, and **[TBC$^{(tBu)4}$P(OH)(OMe)]$^+$**. The last one is reflective of the presence of methanol in the purification steps. Deposition of the same sample from a DCM/MeOH (95:5% v:v) mixture results in the spectrum shown in Fig. 2B. In this case, the intensity of the **[TBC$^{(tBu)4}$P=O]$^+$** peak is significantly reduced and the base peak belongs to the **[TBC$^{(tBu)4}$P(OMe)]$^+$** ion, which apparently originates from the **TBC$^{(tBu)4}$P(OMe)$_2$** molecule which was also observed in the spectrum. It is interesting to note that all known (to date) X-ray crystal structures of phosphorous(V) **TBC^{Rn}** and **TAC^{Rn}** platforms are six-coordinate, which seems to indicate the stabilization of such structures in solution from which all crystals were grown. When vacuum dried sample 2 was deposited on MALDI plate at ambient (humid) atmosphere from regular DCM, the spectrum was dominated by **[TBC$^{(tBu)4}$P]$^+$**, **[TBC$^{(tBu)4}$P=O]$^+$**, and **[TBC$^{(tBu)4}$P(OH)$_2$]$^+$** peaks along with unidentified cluster at 804.3763 *m/z* (Supporting

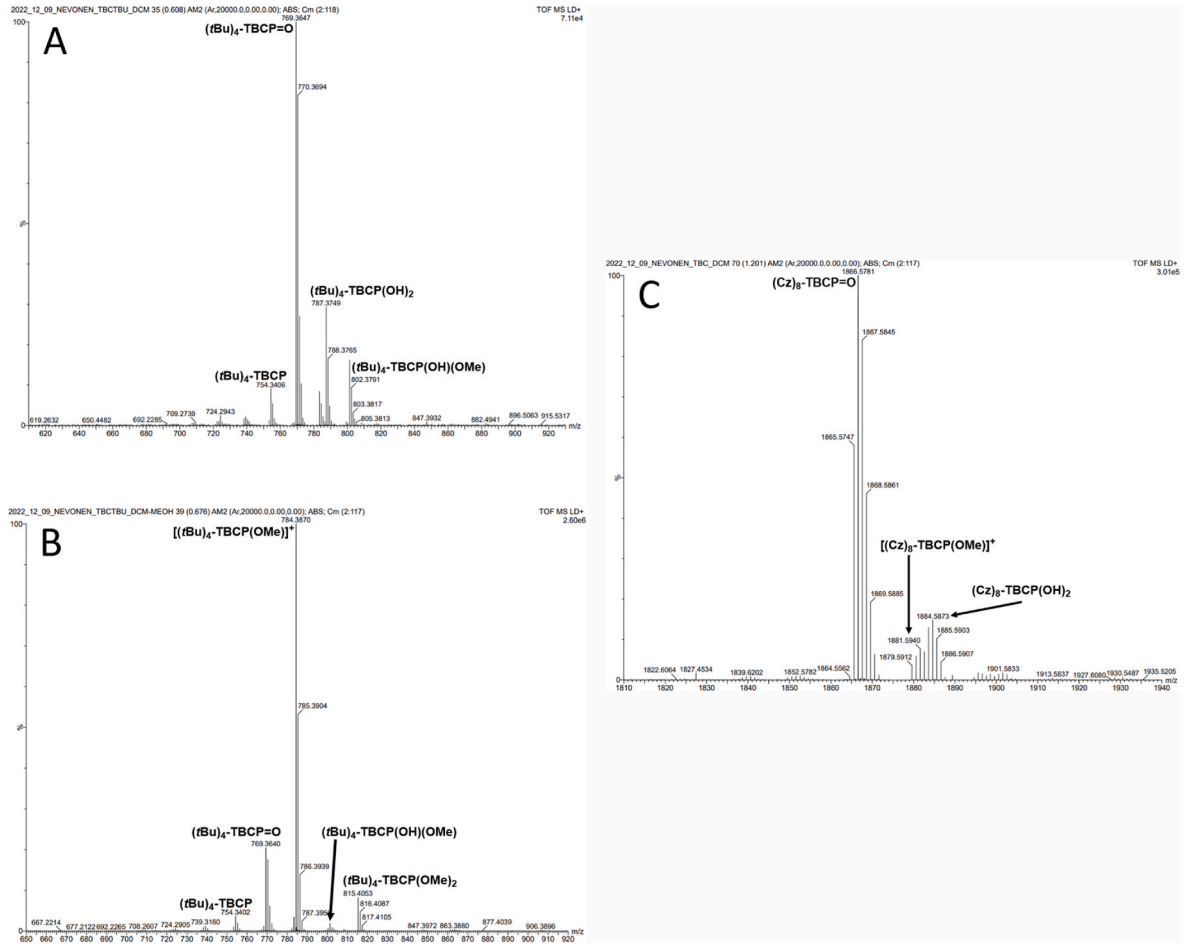

Fig. 2. Matrix-free MALDI-TOF spectra of (A) Sample 1 in DCM, (B) sample 1 in DCM:MeOH (95:5% v:v), (C) **TBC$^{(Cz)8}$P(OH)$_2$** in DCM.

Information Fig. S6A). As expected, the ratio between **[TBC$^{(tBu)4}$P=O]$^+$** and **[TBC$^{(tBu)4}$P(OH)$_2$]$^+$** peaks changes upon addition of the water to DCM. In this case, **[TBC$^{(tBu)4}$P(OH)$_2$]$^+$**cluster dominates the spectrum (Supporting Information Fig. S6B). Finally, when DCM/MeOH (95:5 v/v) mixture was used for deposition of sample 2, the mass spectrum is dominated by **[TBC$^{(tBu)4}$P]$^+$**, **[TBC$^{(tBu)4}$P=O]$^+$**, **[TBC$^{(tBu)4}$P(OH)]$^+$**, **[TBC$^{(tBu)4}$P(OMe)]$^+$**, and **[TBC$^{(tBu)4}$P(OH)(OMe)]$^+$**peaks. Small intensity **[TBC$^{(tBu)4}$P(OMe)$_2$]$^+$** cluster was also observed in the spectrum (Supporting Information Fig. S6C). The low intensity of the **[TBC$^{(tBu)4}$P(OMe)$_2$]$^+$** cluster is indicative of the easiness of dissociation of the axial methoxide anion in the gas phase upon laser irradiation. The high intensities of the **[TBC$^{(tBu)4}$P(OH)(OMe)]$^+$**and **[TBC$^{(tBu)4}$P(OH)$_2$]$^+$**peaks could be indicative of a higher affinity of the OH^- axial ligand compared to MeO^-. This hypothesis correlate well with the observation of both **TBC$^{(tBu)4}$P(OH)(OMe)** (−194.9 ppm) and **TBC$^{(tBu)4}$P(OMe)$_2$** (−187.9 ppm) signals in ^{31}P NMR experiment conducted in $CDCl_3$/MeOH-d4 solution.

Phosphorous 2p XPS data on the room-temperature dried **TBC$^{(tBu)4}$P=O** sample are shown in Supporting Information Fig. S7. On a qualitative level, they correlate well with the XPS spectrum of **TBCP=O** reported by Bender and co-workers [50]. In particular, the main peak at 134.2 eV and shoulder at 135.0 eV have energies close to those observed by Bender and co-workers (~133.8 and ~134.9 eV); however, in order to obtain a reasonable fit, two more peaks were introduced at 133.25 and 134.30 eV. These data, again, might be indicative of the presence of at least two slightly different coordination forms of **TBC$^{(tBu)4}$P** (i.e., **TBC$^{(tBu)4}$P=O** and **TBC$^{(tBu)4}$P(OH)$_2$**), which correlate well with the ^{31}P NMR and MALDI data. Overall, from our and previous data, it is clear that the initially made in pyridine solution **TBC$^{(tBu)4}$P(OH)$_2$** is prone to dehydration in the solid state once subject to thermal and/or vacuum treatment with the formation of **TBC$^{(tBu)4}$P=O** as a final product. However, once in solution, once in solution, **TBC$^{(tBu)4}$P=O** complex prone to form the hexa-coordinated **TBC$^{(tBu)4}$P(OR)$_2$** (R = H or Me) species is evident from ^{31}P NMR and mass spectrometry data. The proposed transformations are outlined in Scheme 1. Similar transformations were already proposed by Goldberg and co-authors [33] for the **TAC^{R8}P(OH)$_2$** compounds, as well as by Longhi and co-authors [74] and Ravikanth and co-authors [59] for the phosphorous(V) corroles.

Next, we collected the UV–Vis and MCD spectra of the **TBC$^{(tBu)4}$P(XY)** complex under different conditions in order to explore the influence of the axial coordination on the (magneto)optical properties of this compound. To the best of our knowledge, this is the first such attempt in the field of triazacorroles and tetrabenzotriazacorroles. The UV–vis and MCD spectra of **TBC$^{(tBu)4}$P(XY)** complexes in the variety of solvents are shown in Fig. 3. In all cases, the UV–vis spectra are dominated by the transitions in the *B*- and *Q*-bands region observed between 400 and 460 nm and 580 and 690 nm, respectively. A strong, red-shifted *B*-band (compared to the phthalocyanine derivatives) is a well-known feature of **TBC** systems [44–50]. The *Q*-band region in **TBC$^{(tBu)4}$P(XY)** has clear solvent dependency. Based on the effective C_{2v} symmetry of the tetrabenzotriazacorrole chromophore, presence of the Q_x and Q_y transitions is expected. In wet pyridine (Fig. 3A), *Q*-band region is dominated by a prominent band at 678 nm with a shoulder observed at 665 nm. Based on the ^{31}P NMR spectroscopy and mass spectrometry, we assign this spectrum to **TBC$^{(tBu)4}$P(OH)$_2$** compound. The *Q*-band region of the UV–Vis spectrum of dry **TBC$^{(tBu)4}$P=O** in dry DCM is dominated by two bands observed at 680 and 661 nm (Fig. 3B). Addition of 5 μL of methanol to this solution leads to the spectrum shown in Fig. 3C. In this

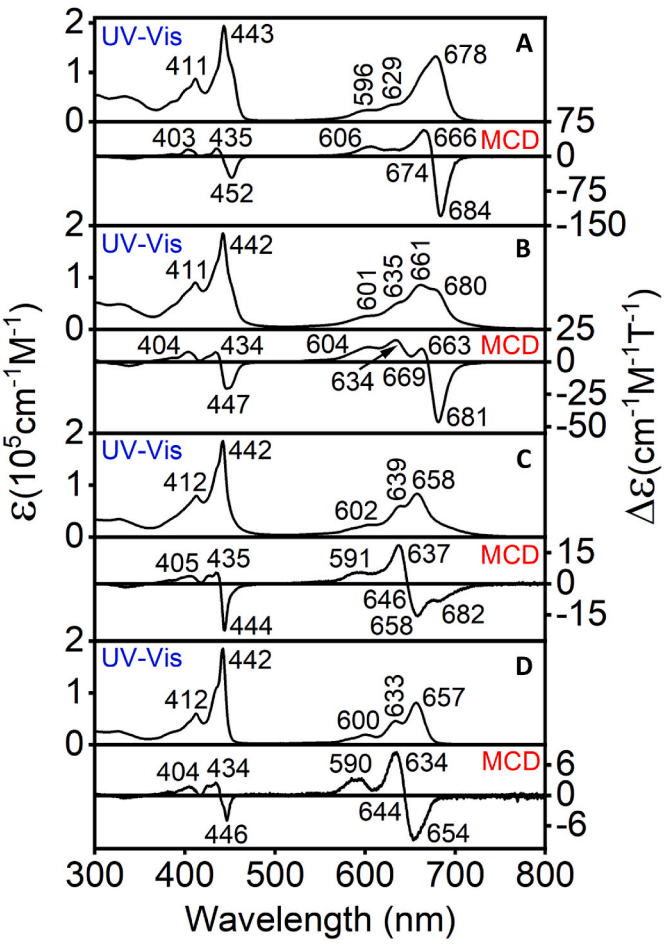

Fig. 3. UV–Vis and MCD spectra of **TBC$^{(tBu)4}$P(OH)$_2$** in pyridine (A); **TBC$^{(tBu)4}$P=O** in dry DCM (B); **TBC$^{(tBu)4}$P(OH)$_2$/TBC$^{(tBu)4}$P(OH)(OMe)/TBC$^{(tBu)4}$P(OMe)$_2$** in DCM/5 μL MeOH (C); **TBC$^{(tBu)4}$P(OMe)$_2$** in DCM/50 μL MeOH (C);.

case, the *Q*-band region is dominated by bands at 658 and 639 nm and a visible shoulder at ~680 nm. This shoulder completely disappears in the presence of 50 μL of methanol (Fig. 3D). In agreement with the ^{31}P NMR and mass spectrometry data, we assign the last spectrum to **TBC$^{(tBu)4}$P(OMe)$_2$** compound. Overall shift of the lowest energy band in this region (Q_x band) is 21 nm (470 cm^{-1}), which is not typical for the transition-metal phthalocyanines and reflective of the axial ligand dependency in tetrabenzotriazacorroles. Interestingly, the most intense transition observed at 442 nm does not have a clear axial ligand dependency. The MCD spectra of **TBC$^{(tBu)4}$P(XY)$_2$** in the *Q*-band region confirms the relatively low (compared to transition-metal phthalocyanines) symmetry of the chromophore. Indeed, in each case, the MCD spectrum in this region is dominated by a pair of Faraday *B*-terms that correlate with the Q_x and Q_y absorption bands. In case of **TBC$^{(tBu)4}$P(OH)$_2$** complex, the pair of Faraday *B*-terms was observed at 684 and 666 nm (Fig. 3A), which is close to B-terms observed for **TBC$^{(tBu)4}$P=O** at 681 and 663 nm (Fig. 3B). However, in case of the **TBC$^{(tBu)4}$P(OMe)$_2$** complex, Q_x and Q_y bands are shifted to 654 and 634 nm (Fig. 3D). Thus, our MCD data also suggest a **TBC$^{(tBu)4}$P=O** ⇌ **TBC$^{(tBu)4}$P(OH)$_2$** ⇌ **TBC$^{(tBu)4}$P(OMe)$_2$** equilibrium in different solvents, which is in agreement with the ^{31}P NMR and mass spectrometry data [74]. Similar behavior was observed but not explained by Kobayashi and Mack for the MCD spectrum of **TBC$^{(α\text{-}BuO)8}$P(OMe)$_2$** complex in which the two lowest energy negative amplitude *B*-terms in the *Q*-band region were clearly split by ~500 cm^{-1} [75]. In this case, the authors should also observe **TBC$^{(α\text{-}BuO)8}$P(OH)$_2$** ⇌ **TBC$^{(α\text{-}BuO)8}$P(OH)(OMe)** ⇌ **TBC$^{(α\text{-}BuO)8}$P(OMe)$_2$** equilibrium upon dissolvation of the initial **TBC$^{(α\text{-}BuO)8}$P(OMe)$_2$** complex in wet solvent. Our observations also correlate well with the MCD spectra of corroles reported by Longhi and co-workers using a DCM/MeOH system [74]. In all cases, pair of *B*-terms has negative-to-positive (in ascending energy) sequence. Following perimeter model [76,77], this is indicative of the ΔHOMO > ΔLUMO (ΔHOMO is the energy difference between Gouterman's a_{1u} and a_{2u} occupied MOs in a standard D_{4h} point group notation and ΔLUMO is the energy difference between Gouterman's pair of e_g unoccupied MOs in a standard D_{4h} point group notation). The ΔHOMO > ΔLUMO ratio was further confirmed by DFT calculations for **TBC^{Rn}P(OH)$_2$** compounds discussed below. Similar to previously reported MCD spectra of phosphorus-centered tetrabenzotriazacorroles [66,69,70,75], the *B*-band region is at a comparable intensity to the *Q*-band region. Furthermore, MCD Faraday pseudo *A*-terms (pairs of closely spaced *B*-terms) are clearly present in the *B*-band region. Overall, our combined ^{31}P NMR, mass spectrometry, and MCD spectroscopy experiments on **TBC$^{(tBu)4}$P(XY)** compounds allowed to explain the behavior of the phosphorous **TBC** compounds in a solid state and solution. Indeed, once dried at elevated temperatures in vacuum, phosphorous **TBCs** can be formulated as penta-coordinated **TBC^{Rn}P=O** complexes. However, these compounds can be easily hydrated in solution with the formation of **TBC^{Rn}P(OH)$_2$** compounds. In the presence of methanol, depending on the methanol concentration, phosphorous **TBCs** can form either **TBC^{Rn}P(OH)(OMe)** or **TBC^{Rn}P(OMe)$_2$** compounds. It also seems that the phosphorous **TBCs** have higher affinity to hydroxide anions compared to the methoxide anions. This behavior mirros that of phosphorous(V) corroles discussed by Ravikanth and co-authors [59].

Synthesis of the novel **TBC$^{(Cz)8}$P(OH)$_2$** compound follows a similar procedure which slightly deviates from Gouterman's procedure [29] *via* the use of a metal-free β,β′-octacarbazole decorated phthalocyanine (H_2PcCz_8).[54] ^{1}H NMR spectra of this compound were recorded in DSMO-d6 at 25 and 90 °C (Supporting Information) and consist of four groups of the aromatic signals. Similar to the previous report on octa-(carbazole)phthalocyanines, a number of overlapped multiplets observed in the solution preclude the accurate peak assignments although confirm the overall number of the aromatic protons in compound. ^{31}P NMR spectrum of this compound in pyridine-d5 (Supporting Information Fig. S1C) has a signal at −198.5 ppm, which is close to that observed in **TBC$^{(tBu)4}$P(OH)$_2$** compound. This observation allows us to confirm its hexacoordinated nature of **TBC$^{(Cz)8}$P(OH)$_2$** in solution. Matrix-free MALDI-TOF spectrum of the **TBC$^{(Cz)8}$P(XY)** air dry sample loaded from regular DCM solution is dominated by the **TBC$^{(Cz)8}$P=O** peak and lower intensity peaks of **TBC$^{(Cz)8}$P(OH)$_2$** and **[TBC$^{(Cz)8}$P(OMe)]$^+$** clusters (Fig. 2C). The presence of the small amount of **[TBC$^{(Cz)8}$P(OMe)]$^+$** cluster can be explained by the presence of MeOH during the purification step and is indicative of much slower axial ligand exchange in more sterically crowded carbazole-substituted compound. Phosphorous 2p XPS data on the room-temperature dried **TBC$^{(Cz)8}$P(OH)$_2$** sample are shown in Supporting Information Fig. S7. On a qualitative level, they correlate well with the XPS spectrum of **TBCP=O** reported by Bender and co-workers [50] and its energies are clearly suggestive of a phosphorous(V) oxidation state; however, at least four peaks are needed to deconvolute the experimental data, which might be indicative of the simultaneous presence of **TBC$^{(Cz)8}$P = O** and **TBC$^{(Cz)8}$P(OH)$_2$** species. Once dried under vacuum at elevated temperature, the elemental analysis of this compound fits well with the penta-coordinated **TBC$^{(Cz)8}$P=O** formula, similar to that reported by Bender and co-workers [50] Thus, again, it seems that the structure of phosphorous (V) **TBC$^{(Cz)8}$P(XY)** samples dried in vacuum under elevated temperature can be formulated as **TBC$^{(Cz)8}$P=O**, while dissolvation of these samples in regular (wet) organic solvents results in a hydration or solvation reaction, leading to the formation of a hexa-coordinated species of general formula **TBC$^{(Cz)8}$P(OR)$_2$** (R = H or Me).

The *Q*-band is significantly red-shifted to 690 nm in the case of **TBC$^{(Cz)8}$P(OH)$_2$** (Fig. 4). This red-shift of the *Q*-band in **TBC$^{(Cz)8}$P(OH)$_2$** is reflective of the electron-donating nature of the eight peripheral

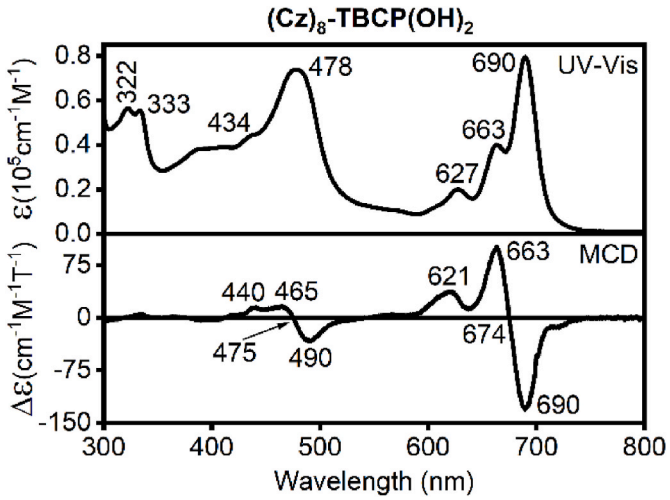

Fig. 4. UV–Vis and MCD spectra of $\mathbf{TBC^{(Cz)8}P(OH)_2}$ in CH_2Cl_2.

carbazole groups. The *B*-band of $\mathbf{TBC^{(Cz)8}P(OH)_2}$ is rather broad and consists of several overlapping transitions centered at 478 nm. Finally, a broad and low intensity band was observed in the UV–vis spectrum in the 520–590 nm region for $\mathbf{TBC^{(Cz)8}P(OH)_2}$, which is absent in the unsubstituted phosphorus-centered **TBC** [29,51,65] UV–vis spectrum. The carbazole groups in $\mathbf{TBC^{(Cz)8}P(OH)_2}$ are electron-donating in nature; therefore, it could be expected that the energies of the carbazole-centered molecular orbitals (MOs) could be near the energy of the tetrabenzotriazacorrole-centered highest occupied molecular orbital (HOMO) which is a π-orbital. For the case of $\mathbf{TBC^{(Cz)8}P(OH)_2}$, low-energy carbazole-to-TBC inter-ligand charge-transfer (ILCT) transitions are expected to appear at larger than *Q*-band energies; therefore, the broad band observed in the UV–vis spectrum of $\mathbf{TBC^{(Cz)8}P(OH)_2}$ in the 520–590 nm region can tentatively be assigned as an ILCT transition. This tentative assignment was further supported by MCD spectroscopy and TDDFT calculations. The *Q*-band region in the MCD spectra of $\mathbf{TBC^{(Cz)8}P(OH)_2}$ is dominated by a pair of intense Faraday MCD *B*-terms centered at 690 and 663 nm. These bands correlate well with the bands at 690 and 663 nm observed in the UV–Vis spectrum. Similar spectroscopic signatures have been observed for a previously reported phosphorus-centered β-octasubstituted tetrabenzotriazacorrole $\mathbf{TBC^{(tBuPhO)8}P(OH)_2}$ species [66]. The intensity of the MCD signals of $\mathbf{TBC^{(Cz)8}P(OH)_2}$ in the 520–590 nm region is quite low, which further supports the tentative ILCT assignment of the ~580 nm transition in $\mathbf{TBC^{(Cz)8}P(OH)_2}$.

The absorption spectra in different solvents of $\mathbf{TBC^{(Cz)8}P(OH)_2}$ and $\mathbf{TBC^{(tBu)4}P(OH)_2}$ complexes are shown in Supporting Information Fig. S8. Furthermore, tracing the *Q*-band's appearance and position at different concentrations was also performed using a range of concentration values (1–9 μM). The $\mathbf{TBC^{(Cz)8}P(OH)_2}$ compound does not show significant solvatochromic behavior in the *Q*-band region. However, the *B*-band profile undergoes an appreciable change as a function of solvent (Supporting Information Fig. S8). Such behavior is not surprising as one might expect that the ILCT transitions should be located in the 400–500 nm region and also, because of their CT nature, the solvatochromic effect should be substantial.

The steady-state fluorescence spectral measurements were conducted for $\mathbf{TBC^{(Cz)8}P(OH)_2}$ and $\mathbf{TBC^{(tBu)4}P(OH)_2}$ in toluene and THF using a xenon lamp. Fig. 5 displays the fluorescence emission of both complexes using different excitation wavelengths (420 and 620 nm). When excited close to the *Q*-band wavelength, the $\mathbf{TBC^{(Cz)8}P(OH)_2}$ and $\mathbf{TBC^{(tBu)4}P(OH)_2}$ compounds display expected emission profiles (Fig. 4). In particular, the main emission peak has a small Stokes shift from the Q_x-band absorption energy, and the energy difference between the main emission peak and vibronic satellite is very close to that observed between the Q_x-band and vibronic satellite in the UV–vis and MCD spectra of the corresponding compounds. When excited at 420 nm, additional very weak bands in the 450–600 nm region were also observed. A similar band was reported for the $\mathbf{TBC^{(SO3H)n}P(OH)_2}$ systems and attributed to the $S_2 \rightarrow S_0$ emission process [68]. The photophysical parameters for $\mathbf{TBC^{(Cz)8}P(OH)_2}$ and $\mathbf{TBC^{(tBu)4}P(OH)_2}$ in toluene and THF are compiled in Table 2. The Φ_F of the carbazolyl substituted $\mathbf{TBC^{(Cz)8}P(OH)_2}$ compound in two different solvents examined herein are generally higher than the analogous metal-free phthalocyanine precursor [54]. The Φ_F values obtained for $\mathbf{TBC^{(Cz)8}P(OH)_2}$ after excitation at 420 nm are larger by a factor of two (0.41) than that obtained after excitation at 620 nm (0.20) in both solvents (toluene and THF), and this was attributed to an ILCT transition caused by the carbazole groups. Meanwhile, the Φ_F for $\mathbf{TBC^{(tBu)4}P(OH)_2}$ after excitation at 420 nm shows little change (0.30–0.27) compared to excitation at 620 nm (0.25–0.24) either in toluene or THF, respectively, as shown in Table 2.

The fluorescence lifetimes (τ_F) and their kinetic decay for both complexes were studied using different excitation wavelengths in both THF and toluene, as shown in Table 2 and Fig. S11. Time-correlated single photon counting (TCSPC) for $\mathbf{TBC^{(Cz)8}P(OH)_2}$ generated a short-lived decay (~2 ns) as a major lifetime in either solvent. A second minor lifetime was also observed (~12 ns). The fluorescence lifetime obtained for $\mathbf{TBC^{(tBu)4}P(OH)_2}$ in both solvents was slightly longer compared to that of $\mathbf{TBC^{(Cz)8}P(OH)_2}$, with a lifetime ~0.9 ns (42%) and longer components of ~3 ns in THF and 12 ns in low polarity toluene (>50%). The additional decay time in **TBCs** that were excited in 400–450 nm region have been reported earlier for a number of compounds. At this moment, no rational explanation on such photophysical behavior exists in the literature. Nanosecond transient absorption spectra were studied to confirm the triplet state production for $\mathbf{TBC^{(Cz)8}P(OH)_2}$ and $\mathbf{TBC^{(tBu)4}P(OH)_2}$ as shown in Fig. 6. For $\mathbf{TBC^{(Cz)8}P(OH)_2}$, a significant ground state bleaching bands at 490 and 690 nm was observed upon photoexcitation. In addition, a raise of a slow (μs regime)

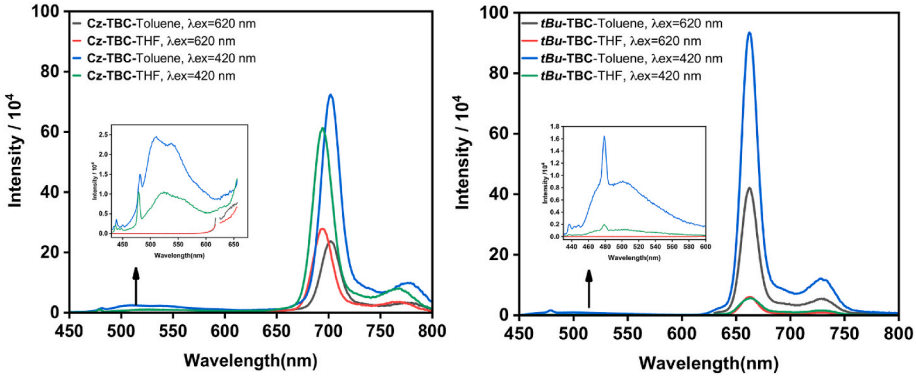

Fig. 5. Emission spectra of $\mathbf{TBC^{(Cz)8}P(OH)_2}$ (left) and $\mathbf{TBC^{(tBu)4}P(OH)_2}$ (right) in toluene and THF using different excitation wavelengths (420 nm and 620 nm).

Table 2
Photophysical data[a] of **TBC$^{(Cz)8}$P(OH)$_2$** and **TBC$^{(tBu)4}$P(OH)$_2$** complexes in both THF and toluene.

Compound	Solv.	λ_{ex} (nm)	Abs. Maxima (nm)	Log (ε)Q-Band	λ_F (nm)	Φ_F	τ_F (ns)
TBC$^{(Cz)8}$P(OH)$_2$	THF	420	322, 335, 461, 473, 615, 643, 685	4.9	509, 540, 702, 778	0.41	τ_1 = 2.09 (91%) τ_2 = 13.65 (9%)
		620			702, 778	0.20	τ_1 = 2.88 (100%)
	Tol.	420	322, 335, 463,493, 625, 656,692	5.0	524, 692, 768	0.41	τ_1 = 1.45 (96%) τ_2 = 0.65 (4%)
		620			692, 768	0.20	τ_1 = 2.68 (100%)
TBC$^{(tBu)4}$P(OH)$_2$	THF	420	326, 410, 461,596, 625, 642	4.9	545, 663, 730	0.27	τ_1 = 0.92 (42%) τ_2 = 3.31 (58%)
		620			662, 730	0.24	τ_1 = 3.66 (100%)
	Tol.	420	327, 412, 473, 603, 637, 663	4.9	545, 661, 730	0.30	τ_1 = 3.36 (33%) τ_2 = 12.88 (67%)
		620			662, 730	0.25	τ_1 = 3.40 (100%)

[a] Q-band absorption maximum (λ_{max}), extinction coefficient (ε), emission maximum (λ_F), fluorescence lifetime (τ_F), and fluorescence quantum yield (Φ_F).

decaying broad bands appeared between 400 and 450 nm, 510 and 600 nm, as well as 710 and 750 nm due to the formation of a triplet state in the carbazolyl complex (Fig. 6, left). These bands were assigned to the $T_1 \rightarrow T_n$ transitions in unsubstituted and sulfonated phosphorous(V) **TBCs** [68]. For **TBC$^{(tBu)4}$P(OH)$_2$** the dynamics of the ground state bleaching bands at 450 and 660 nm correlate with the formation of slow decaying bands between 350 and 370 nm, 460 and 570 nm, as well as 710 and 750 nm that are associated with the formation of a triplet state in this molecule [23]. Again, these bands can be assigned to the $T_1 \rightarrow T_n$ transitions similar to those in unsubstituted and sulfonated phosphorous (V) **TBCs** [68]. The triplet state lifetime was detected in both air and argon. Our results show that the carbazole substituents, in the case of **TBC$^{(Cz)8}$P(OH)$_2$**, increase the triplet state lifetime to 112 μs compared to the **TBC$^{(tBu)4}$P(OH)$_2$** which possess a shorter triplet lifetime (91 μs) in argon.

The electrochemical behavior of tetrabenzotriazacorroles **TBC$^{(Cz)8}$P(OH)$_2$** and **TBC$^{(tBu)4}$P(OH)$_2$** was investigated with cyclic voltammetry (CV) and differential pulse voltammetry (DPV) methods using a DCM/0.1 M tetrabutylammonium perchlorate (TBAP) system (Fig. 7 and Supporting Information Figs. S13 and S14).

Regarding the **TBC$^{(Cz)8}$P(OH)$_2$** compound, two oxidation processes were observed within the electrochemical window at 0.23 and 0.43 V (vs. Fc/Fc$^+$) with the first oxidation event being reversible and the second one irreversible. The reduction window of **TBC$^{(Cz)8}$P(OH)$_2$** shows two irreversible reduction processes observed at −1.24 and −1.74 V (Fc/Fc$^+$). All redox events were assigned to oxidation and reduction of the tetrabenzotriazacorrole core. Interestingly, the octacarbazole-based multielectron oxidation event typically observed at higher potentials in carbazole-containing phthalocyanines (Pcs) [24,33] was not observed in **TBC$^{(Cz)8}$P(OH)$_2$**. For compound **TBC$^{(tBu)4}$P(OH)$_2$**, two closely spaced quazi-reversible oxidation events were observed at

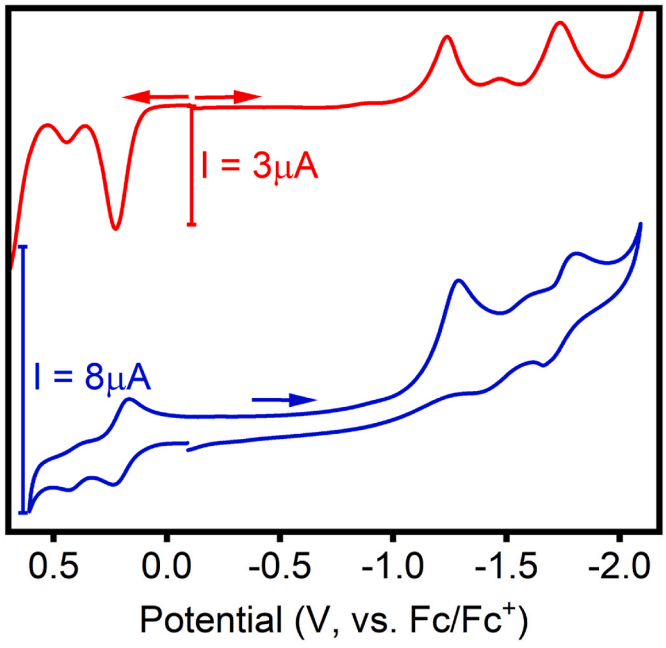

Fig. 7. Electrochemical CV (blue) and DPV (red) voltammograms for **TBC$^{(Cz)8}$P(OH)$_2$** in a DCM/0.1 M TBAP system.

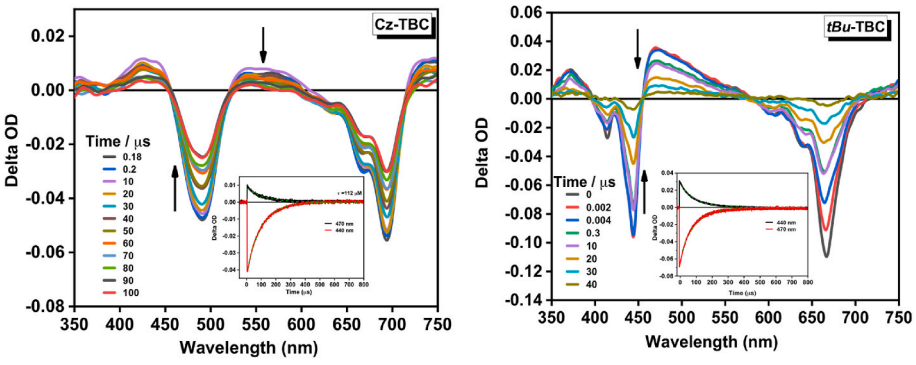

Fig. 6. Nanosecond time-resolved transient difference absorption spectra of (left) **TBC$^{(Cz)8}$P(OH)$_2$** and (right) **TBC$^{(tBu)4}$P(OH)$_2$**. Inset: decay trace of the transients of **TBC$^{(Cz)8}$P(OH)$_2$** and **TBC$^{(tBu)4}$P(OH)$_2$** in argon saturated solution. Excited with nanosecond pulsed laser with A_{OD}~ 0.5 in deaerated toluene.

slightly lower potentials (−0.10 and 0.20 V) than for **TBC$^{(Cz)8}$P(OH)$_2$**. Titration of DCM solution of **TBC$^{(tBu)4}$P(OH)$_2$** with methanol (0–10% v/v, Supporting Information Fig. S13) results in the formation of **TBC$^{(tBu)4}$P(OMe)$_2$** (as discussed in ^{31}P NMR section above), which has the first oxidation potential shifted to 0.00 V with the second oxidation potential remained unaffected. The 100 mV shift of the first oxidation potential between **TBC$^{(tBu)4}$P(OH)$_2$** and **TBC$^{(tBu)4}$P(OMe)$_2$** correlates well with the 0.06 eV blue shift of the Q_x band observed for the same transformation. The two closely spaced oxidation events in triazacorroles have already been reported [58]. The reduction window of **TBC$^{(tBu)4}$P(OH)$_2$** displays two irreversible reduction events at very anodic potentials (−1.60 and −2.15 V).

In order to confirm the oxidation site in **TBC$^{(Cz)8}$P(OH)$_2$** and **TBC$^{(tBu)4}$P(OH)$_2$**, we conducted spectroelectrochemical oxidation of these compounds using a DCM/0.3 M TBAP system (Fig. 8). In the case of **TBC$^{(Cz)8}$P(OH)$_2$**, oxidation under spectroelectrochemical conditions results in the reduction of the *Q*- and *B*-band intensities, which is accompanied by the formation of bands at 543, 792, and 946 nm (Fig. 8). The NIR band at 792 nm (and similar band at 753 nm was observed in the oxidation of **TBC$^{(tBu)4}$P(OH)$_2$**) is indicative of the formation of a **[TBC$^{(Cz)8}$P(OH)$_2$]$^{+\cdot}$** species in solution [54,55]. The nature of new 946 nm band in the UV–Vis–NIR spectrum of **[TBC$^{(Cz)8}$P(OH)$_2$]$^{+\cdot}$** remains unclear but might be associated with carbazole-to-SOMO inter-ligand charge-transfer process. In agreement with the electrochemical data, the oxidation is reversible. Indeed, the **[TBC$^{(Cz)8}$P(OH)$_2$]$^{+\cdot}$** species can be almost completely transformed back to the starting **TBC$^{(Cz)8}$P(OH)$_2$** compound (Supporting Information Fig. S15). In contrary, although the formation of new bands at 542 and 753 nm was observed upon oxidation of the **TBC$^{(tBu)4}$P(OH)$_2$** compound under spectroelectrochemical conditions, this process was found to be irreversible in our spectroelectrochemical cell which typically requires 40–60 min for complete oxidation (Fig. 8 and Supporting Information Fig. S15). We speculate that the eight bulky carbazole groups present in the **TBC$^{(Cz)8}$P(OH)$_2$** compound prevent the **[TBC$^{(Cz)8}$P(OH)$_2$]$^{+\cdot}$** species from interacting with the solvent molecules which might result in sample degradation.

DFT and TDDFT Calculations. The vertical excitation energies and electronic structures of tetrabenzotriazacorroles **TBC$^{(Cz)8}$P(OH)$_2$** and **TBC$^{(tBu)4}$P(OH)$_2$** were investigated by DFT and TDDFT calculations. In order to correlate the DFT and TDDFT results with experimental redox properties and UV–vis spectra, the polarized continuum model (PCM) was utilized to account for solvent effects (chloroform was used as the solvent for all calculations). Since the calculated singlet-triplet gaps and TDDFT-predicted vertical excitation energies are expected to have exchange-correlation dependencies [78–81], we tested the B3LYP, HSEH1PBE, and MN12SX functionals. It was found that all three functionals provide similar electronic structures and singlet-triplet energy gaps for the **TBC$^{(Cz)8}$P(OH)$_2$** and **TBC$^{(tBu)4}$P(OH)$_2$** compounds, and thus, only one set of calculations will be discussed in detail below. The energy level diagrams for **TBC$^{(Cz)8}$P(OH)$_2$** and **TBC$^{(tBu)4}$P(OH)$_2$** as predicted by DFT-PCM calculations are shown in Fig. 9, and the selected frontier molecular orbital (MO) profiles are depicted in Fig. 10, S16, and S17.

In both compounds, the DFT-predicted HOMO takes the form of Gouterman's a_{1u} orbital (in standard D_{4h} symmetry notation) [82–84], with significant electron density contributions from the pyrrolic α- and β-carbon atoms. In the case of **TBC$^{(Cz)8}$P(OH)$_2$**, DFT predicts that the electron density distributions on HOMO-1 to HOMO-16 remain largely localized on the carbazole moieties, while HOMO-17 resembles Gouterman's a_{2u} orbital with additional electron density present on the inner- and *meso*-nitrogen atoms of the tetrabenzotriazacorrole core. The energy differences between Gouterman's a_{1u} and a_{2u} orbitals that were predicted by DFT are about half that of typical phthalocyanines at about 1.2 and 0.8 eV for **TBC$^{(Cz)8}$P(OH)$_2$** and **TBC$^{(tBu)4}$P(OH)$_2$**, respectively, and the carbazole-based HOMO-1 to HOMO-16 orbitals are also energetically closely spaced (~0.5 eV, Fig. 8). The LUMO and LUMO+1 as predicted by DFT in compounds **TBC$^{(Cz)8}$P(OH)$_2$** and **TBC$^{(tBu)4}$P(OH)$_2$** also resemble the classical Gouterman's pair of e_g orbitals, which are dominated by electron density contributions from α- and β-pyrrolic carbons, inner- and *meso*-nitrogen atoms, and the benzene ring of the triazatetrabenzcorrole core (Fig. 10). Overall, the electronic structures of compounds **TBC$^{(Cz)8}$P(OH)$_2$** and **TBC$^{(tBu)4}$P(OH)$_2$** that were predicted by DFT correlate well with the electrochemical and spectroscopic data that were collected. To be more specific, based on the DFT calculations, it is expected that the first two oxidations will be centered on the tetrabenzotriazacorrole core and this notion is well-correlated with the spectroelectrochemical and electrochemical data collected on **TBC$^{(Cz)8}$P(OH)$_2$** and **TBC$^{(tBu)4}$P(OH)$_2$**. Additionally, the DFT calculations are indicative of a tetrabenzotriazacorrole-centered lowest-energy excited state, while many of the ILCT transitions can be expected in the spectral envelope containing energies higher than that of the *Q*-band. Finally, DFT predicts a ΔHOMO > ΔLUMO relationship for both compounds (ΔHOMO is the energy difference between the a_{1u} and a_{2u} MOs and ΔLUMO is the energy difference in e_g set of MOs). According to the perimeter model [76,77], this should lead to the negative-to-positive (in ascending energy) sequence in the *Q*-band region, which indeed is observed experimentally. Reported earlier kinetics of the photodynamic quenching of organic molecules by **TBCs** [53] suggests that the triplet state in these platforms is 0.54 eV lower than the first excited singlet state. Our DFT calculations, using all three exchange-correlation functionals, indeed predicted a 0.66–0.97 eV gap between the first excited singlet state and the triplet state (Supporting Information Table S1).

The TDDFT-predicted UV–vis spectra of **TBC$^{(Cz)8}$P(OH)$_2$** and **TBC$^{(tBu)4}$P(OH)$_2$** are presented in Fig. 11 and S19, while the summary of excited state contributions for the most intense excited states is listed in Table S2.

Generally, the TDDFT results agree well with both the experimental UV–vis spectra and electronic structures of compounds **TBC$^{(Cz)8}$P(OH)$_2$**

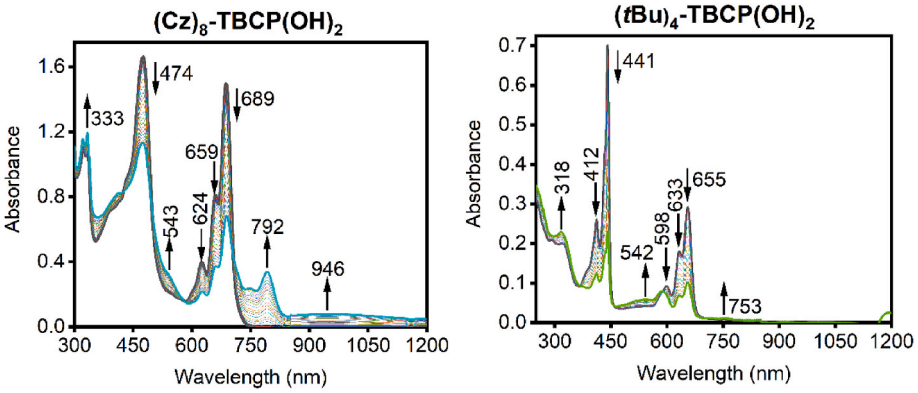

Fig. 8. Spectroelectrochemical oxidation of **TBC$^{(Cz)8}$P(OH)$_2$** and **TBC$^{(tBu)4}$P(OH)$_2$** using a DCM/0.3 M TBAP system.

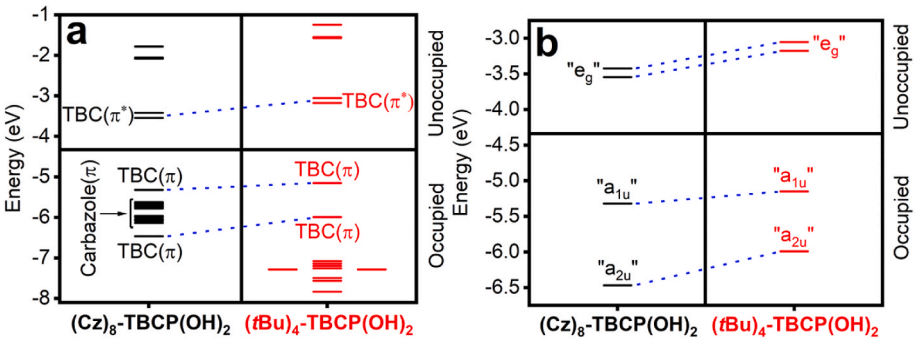

Fig. 9. DFT-PCM predicted energy level diagram for (a) select frontier molecular orbitals and (b) Gouterman's classical frontier orbitals.

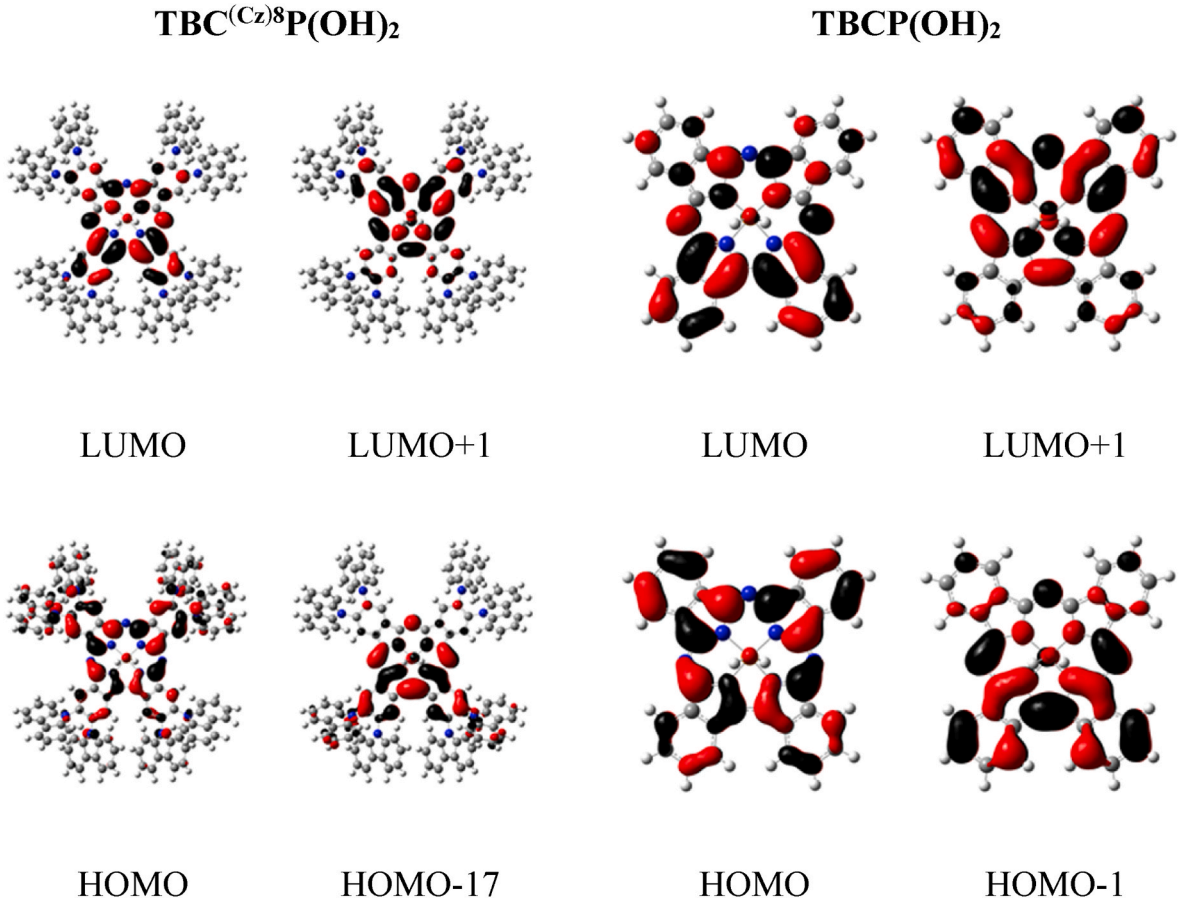

Fig. 10. DFT-PCM predicted images of Gouterman's classic frontier orbitals of **TBC$^{(Cz)8}$P(OH)$_2$** (left) and **TBCP(OH)$_2$** (right).

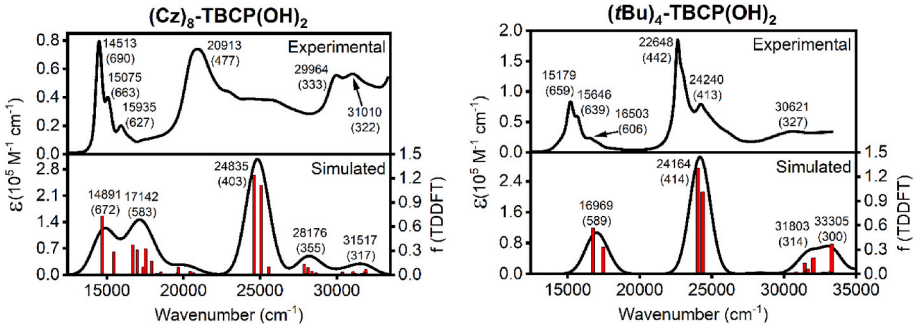

Fig. 11. Experimental (upper) and TDDFT-predicted (lower) UV–vis spectra of **TBC$^{(Cz)8}$P(OH)$_2$** and **TBC$^{(tBu)4}$P(OH)$_2$** using the HSEH1PBE/LANL2DZ-PCM method.

and **TBC$^{(tBu)4}$P(OH)$_2$**. Particularly, the first few excited states of **TBC$^{(Cz)8}$P(OH)$_2$** and **TBC$^{(tBu)4}$P(OH)$_2$** that were predicted by TDDFT and comprise the *Q*-band region are singly-degenerate transitions of moderate intensity which are dominated by H→L and H→L+1 single-electron excitations. The non-degeneracy of these excited states differs from those of analogous phthalocyanine compounds due to the lower degree of molecular symmetry which is a result of the "missing" *meso*-nitrogen atom on the tetrabenzotriazacorrole framework relative to the *Pc* structure. In the case of **TBC$^{(Cz)8}$P(OH)$_2$** and absent from **TBC$^{(tBu)4}$P(OH)$_2$** are the several TDDFT-predicted ILCT bands, which are largely dominated by carbazole-based single-electron excitations of the HOMO-1 to HOMO-16 orbitals to higher-energy carbazole-centered and unoccupied triazatetrabenzcorrole (LUMO and LUMO+1) orbitals. These excitations have clear ILCT character, while their intensities are overestimated in TDDFT calculations (which is quite typical for hybrid exchange-correlation functionals). Also, the TDDFT results indicate large HOMO-17→LUMO, LUMO+1 (for **TBC$^{(Cz)8}$P(OH)$_2$**) and HOMO-1→LUMO, LUMO+1 (for **TBC$^{(tBu)4}$P(OH)$_2$**) contributions to the most intense *B*-band region transitions. Overall, the TDDFT results indicate TBC-centered excited states at low energy, followed by the expected ILCT transitions.

3. Conclusion

Two phosphorus-centered tetrabenzotriazacorrole compounds were prepared and investigated from an electronic structure standpoint where structure **TBC$^{(Cz)8}$P(OH)$_2$** possessed eight peripheral carbazole substituents and **TBC$^{(tBu)4}$P(OH)$_2$** was decorated with four peripheral *tert*-butyl groups. Overall, the UV–vis and MCD spectra for **TBC$^{(Cz)8}$P(OH)$_2$** and **TBC$^{(tBu)4}$P(OH)$_2$** appeared quite similar with the exception of the red-shifted and more intense *Q*-band for **TBC$^{(Cz)8}$P(OH)$_2$**. Based on the ^{31}P NMR, mass spectrometry, UV–Vis, and MCD data, it was demonstrated that the initial pentacoordinated **TBC$^{(tBu)4}$P=O** complex can be easily transformed to the hexa-coordinated species in water and methanol following **TBC$^{(tBu)4}$P=O** ⇌ **TBC$^{(tBu)4}$P(OH)$_2$** ⇌ **TBC$^{(tBu)4}$P(OH)(OMe)** ⇌ **TBC$^{(tBu)4}$P(OMe)$_2$** equilibrium. The UV–vis spectra were accurately simulated for both compounds using a TDDFT approach. For **TBC$^{(Cz)8}$P(OH)$_2$**, the electrochemical experiments detected two oxidation and reduction processes. The electrochemical analysis of **TBC$^{(tBu)4}$P(OH)$_2$** uncovered two partially overlapping oxidation processes and two partially reversible reduction events. It was found that for **TBC$^{(tBu)4}$P(OH)$_2$**, addition of methanol to the electrolyte/sample solution caused the two oxidation processes to shift closer together as a result of the axial hydroxy groups being replaced by methoxy groups. The spectroelectrochemical oxidation performed on **TBC$^{(tBu)4}$P(OH)$_2$** was found to be completely irreversible but fully reversible for **TBC$^{(Cz)8}$P(OH)$_2$**. Also, for **TBC$^{(Cz)8}$P(OH)$_2$**, the spectroelectrochemical data showed the characteristic feature of a cationic radical species *via* the broad low-energy signal at 792 nm; this feature was observed for **TBC$^{(tBu)4}$P(OH)$_2$** at 753 nm. Finally, the DFT-predicted energy level diagram of **TBC$^{(Cz)8}$P(OH)$_2$** showed several carbazole-centered molecular orbitals that were energetically intermixed with the Gouterman's frontier a_{1u} and a_{2u} orbitals; however, for **TBC$^{(tBu)4}$P(OH)$_2$**, the four Gouterman's frontier orbitals were predicted to be energetically sequential as the *tert*-butyl substituents behaved quite innocently with negligible contribution to the electronic structure. Transient absorption spectroscopy was monitored to investigate the triplet state formation and lifetimes (τ_T) which were 112 μs for **TBC$^{(Cz)8}$P(OH)$_2$** and 91 μs for **TBC$^{(tBu)4}$P(OH)$_2$**. The axial ligand exchange dynamics investigation revealed that the phosphorus center is highly prone to coordination and, based on the mass spectrometry results, a mixture of axially coordinated products was observed which included different configurations of hydroxy, methoxy, or pyridine axial coordination. The results reveal that our novel phosphorus corroles can be developed as a new type of efficient triplet photosensitizer for various applications.

4. Experimental section

4.1. General methods

The starting materials were prepared according to our previously reported method to prepare metal-free phthalocyanine [54]. Column chromatography was performed using Merck silica gel 60 of mesh size 0.040–0.063 mm. Anhydrous solvents were either supplied from Sigma-Aldrich and used as they were received or dried as described by Perrin and Armarego [85]. ^{1}H and ^{13}C NMR spectra were performed using a Bruker DPX 600 at 600 MHz and 150 MHz, respectively. UV–Vis spectra were recorded in $CHCl_3$, DCM, DMSO, THF and toluene using a Varian Cary 5000 spectrometer and a Shimadzu UV-2600 spectrophotometer. Elemental analyses were performed on an Elementar Vario MICRO Cube and analyzed using W-positive mode in the range of 1000–3000 *m/z*. Capillary and sample cone voltages were set at 4800 and 174 V, respectively. Desolvation and cone gas were 500 and 50 L h^{-1}. The desolvation temperature was 225 °C and the ion source temperature was 120 °C. In addition, clusters of peaks that corresponded to the calculated isotope composition of the molecular ion were observed by matrix-assisted laser desorption/ionization-time-of-flight mass spectrometry (MALDI-TOF) *via* an ultrafleXtreme (Bruker). The MALDI-TOF mass data for samples are presented as the mass of the most intense peak in the cluster instead of the exact mass.

4.2. Fluorescence measurements

Steady-state and time-resolved fluorescence were measured at room temperature using an Edinburgh Instruments FLS980 spectrofluorometer equipped with a 450 W xenon lamp. The samples were excited at 420 nm and 620 nm.

4.3. Fluorescence quantum yields (ΦF)

The fluorescence quantum yields were acquired using an integrating sphere incorporated into a spectrofluorometer (FLS980, Edinburgh Instruments) using Eq. (1) and Eq. (2)

$$\Phi_F^X = \frac{L_{sam}}{E_{ref} - E_{sam}}(\%) \tag{1}$$

corrected to re-absorption by:

$$\Phi_F = \frac{\Phi_F^X}{1 - a + a\,\Phi_F^X/100}(\%) \tag{2}$$

where L_{Sam} is the area under the detected spectrum in the part of the spectrum where sample emission occurs, E_{Ref} is the area under the reflection part of the detected spectrum using pure solvent as reference material (diffuse reflectance), E_{Sam} is the area under the reflection part of the detected spectrum after absorption by the sample, and a is the reabsorbed area.

4.4. Time-resolved spectroscopy measurements

The time-resolved spectrosopy measurements were performed using the time-correlated single-photon-counting technique (TCSPC) integrated in the Edinburgh Instruments' FLS-980 fluorescence spectrometer equipped with a Supercontinuum Fianium White Laser as the excitation source at 420 nm and 620 nm (frequency of 10 MHz). The instrument response function was measured using a diffusive reference sample (LUDOX ® from Sigma-Aldrich). Reconvolution fit analysis software (FLS980, Edinburgh Instruments) was used for lifetime data analysis.

4.5. Nanosecond transient absorption spectroscopy

The nanosecond time-resolved transient absorption spectra were measured with laser flash photolysis using an Edinburgh Instruments LP980 instrument in degassed solution (prepared by bubbling with argon for 20 min). The samples were excited with a continuum Surelite laser (420 nm) as the excitation source. The analyzing light was produced by a pulsed xenon lamp. The laser and analyzing light beams perpendicularly passed through a quartz cell with an optical path length of 1 cm. The signal was displayed and recorded on a Tektronix MDO 3022 Mixed Domain Oscilloscope and a PMT-LP detector. The laser energy incident at the sample was attenuated to ca. 20± mJ per pulse. Time profiles at a series of wavelengths from which point-by-point spectra were assembled were recorded with the aid of a PC controlled kinetic absorption spectrometer. The lifetimes were obtained with the LP980 software. The concentrations of the target compounds were typically 20 μM providing $A_{420} = 0.45$ in a 1 cm cuvette.

4.6. Synthesis and characterization

Synthesis of TBC$^{(Cz)8}$P(OH)$_2$. TBC$^{(Cz)8}$P(OH)$_2$ had been synthesized from the corresponding octa-carbazole substituted metal-free phthalocyanine precursor [54] (**Pc^{Cz8}H$_2$**) according to the general procedure [29] as follows: 0.6 g of **Pc^{Cz8}H$_2$** (1.17 mmol) in 10 mL of pyridine was added into a 50 mL three-necked round-bottomed flask, which was equipped with a reflux condenser and a gas inlet tube. Pyridine (5 mL) that contained 3.2 mL of PBr_3 (35 mmol) was then added and the resulting mixture was heated at 90–100 °C and stirred for 2 h. After cooling, the mixture was poured into water and filtered, the solid was washed thoroughly with water. The crude product was dissolved in pyridine and purified by column chromatography ($CHCl_3$–MeOH in 9:1 ratio). Yield: 51%. ^{1}H NMR (DMSO-d_6): ^{1}H NMR (DMSO-d_6): δ = 8.56 (s, 4H), 8.1–8.3 (m, 16H), 7.55–7.6 (m, 12H), 7.35–7.45 (m, 40H). ^{31}P NMR (Py-d5): δ = −198.53. UV–Vis [CH_2Cl_2; λ, nm (log ε, cm^{-1} M^{-1})]: 478 (4.87), 627 (4.30), 663 (4.60), 690 (4.90). MS (MALDI-TOF), molecular ion = 1884.59 *m/z* in a MeOH-free system and 1912.62 *m/z* in a MeOH-containing system. Elemental analysis for vacuum dried at 100 °C sample: calculated for $C_{128}H_{72}N_{15}O_1P_1$: C – 82.34%; H – 3.89%; N - 11.25%; found: C – 82.33%; H – 3.97%; N – 11.23%.

4.7. Synthesis of Pc$^{(tBu)4}$H$_2$

40 mL of dry *N*,*N*-dimethylaminoethanol and 5 g (27.1 mmol) of 4-*tert*-butyl-phthalonitrile were placed into a 50 mL 3-neck round-bottom flask fitted with a water condenser and charged with a magnetic stir bar. Under an argon atmosphere, 0.6 eq. (374 mg) of elemental sodium was added to the mixture before refluxing for 30 min. The bulk of the solvent was then evaporated and the remaining mixture crystallized in water. After filtering and drying, the crystals were dissolved in DCM and run through a silica flash column and eluted with DCM. The product was recrystallized in a 4:1 EtOAc:DCM system with a 24% yield.

4.8. Synthesis of TBC$^{(tBu)4}$P(XY) derivatives

100 mg (0.14 mmol) of **Pc$^{(tBu)4}$H$_2$** was added to 10 mL of pyridine in a Schlenk flask and 25 eq. (284 μL) of PBr_3 was added. This mixture was heated to 90-100°C and stirred for 75 min under an argon atmosphere. The reaction mixture was then crystallized in ice-water, filtered, and dried. Two methods were used in purification. Sample 1 was initially dissolved in DCM, filtered, and the filtrate was purified using first column chromatography (silica gel; 100–95 DCM 0–5 MeOH gradient solvent mixture as eluent). Dark blue fraction was collected, solution was evaporated using rotary evaporator, and the resulting residue was dried at room temperature. According to ^{31}P NMR data (major peak at −187 ppm and the minor peak at −194.8 ppm) this sample is dominated by **TBC$^{(tBu)4}$P(OMe)$_2$** with a minor contribution from **TBC$^{(tBu)4}$P(OH)(OMe)**. Yield: 22%. Sample 2 was purified using first column chromatography (silica gel; 85:15 v/v DCM:THF solvent mixture as eluent). Further purification was performed *via* silica preparative TLC using a 5:1 v/v DCM:THF system. Dark blue fraction was collected, solution was evaporated using rotary evaporator, and the resulting residue was dried at 100 °C overnight. Yield: 34%. According to ^{31}P NMR spectra, this sample is pure **TBC$^{(tBu)4}$P=O**. ^{1}H NMR ($CDCl_3$): δ 9.44 (m, 8H), 8.40 (m, 4H), 1.70 (s, 9H), 1.63 (m, 27H). UV–Vis [CH_2Cl_2; λ, nm (log ε, cm^{-1} M^{-1})]: 443 (4.27) Due to observed ligand exchange dynamics, the molar absorptivity coefficients for the signals in the *Q*-band region are inconsistent and therefore, not listed herein. MS (MALDI-TOF), molecular ion = 787.37 *m/z* in a MeOH-free system and 815.41 *m/z* in a MeOH-containing system.

4.9. UV–vis/MCD spectroscopy

All UV–vis spectra were collected on an Agilent Cary 5000 spectrophotometer and MCD spectra were measured with a Jasco J-1500 CD spectrometer using a Jasco MCD-581 electromagnet operated at 1.0 T. The completed MCD spectra were measured at 10 °C in parallel and antiparallel orientations with respect to the magnetic field.

4.10. Electrochemical measurements

The electrochemical data were collected using a CH-620 analyzer with either glassy carbon or platinum working, platinum auxiliary, and Ag/AgCl pseudo-reference electrodes. Decamethylferrocene was used as an internal standard for the studied complexes and the reported potentials were corrected to the Fc/Fc $^+$ couple. All electrochemical experiments were conducted in a CH_2Cl_2/0.1 M tetrabutylammonium perchlorate (TBAP) system.

4.11. Spectroelectrochemical measurements

The spectroelectrochemical experiments were performed using a Jasco V-770 UV–vis–NIR spectrophotometer in tandem with a CH Instruments electrochemical analyzer which was operated using the bulk electrolysis mode. The data were collected using a custom-made 1 mm cell, a platinum mesh working electrode, platinum auxiliary electrode, Ag/AgCl pseudo-reference electrode, and a 0.3 M solution of TBAP in CH_2Cl_2.

4.12. Computational details

All calculations were run using Gaussian 16 [86]. The B3LYP [87,88], HSEH1PBE [89], or MN12SX [90] exchange-correlation functional with the LANL2DZ basis set [91] were used for all calculations. Vibrational frequencies were calculated to ensure all geometries were local minima. All calculations were conducted in solution using the PCM model [92], with chloroform as the solvent. For all TDDFT-PCM calculations, 100 excited states were predicted for each compound. The QMForge program [93] was used for the orbital analysis.

Authors contributions

Dr. Ghazal synthesized octacarbazoletetrabenzotriazacorrole and measured solvatochromic UV–Vis, ^{1}H and ^{31}P NMR spectra of this compound. Dr. Nevonen synthesized tetra-*tert*-butyltetrabenzotriazacorrole, characterized it, conducted all MCD, electro-and spectroelectrochemical experiments, and analyzed computational data. Dr. Shuaib and Salah collected and analyzed photophysical data. Dr. Ghazal and Dr. Nevonen drafted the manuscript. Professor Makhseed and Nemykin designed the project and edited the manuscript. Professor Nemykin conducted all DFT and TDDFT calculations.

Declaration of competing interest

The authors declare that they have no known competing financial interests or personal relationships that could have appeared to influence the work reported in this paper.

Data availability

Data will be made available on request.

Acknowledgement

The authors are gratefully acknowledging Kuwait Foundation for the Advancement of Science (project PR 18-12SC01) and the RSP unit general facilities of the Faculty of Science GFS (GS 01/01, GS 02/01, GS 03/01, GS 01/03, GS 01/05, GS 01/08, and GS 02/13). NSF support for VNN (CHE-2153081) is greatly appreciated.

Appendix A. Supplementary data

Supplementary data to this article can be found online at https://doi.org/10.1016/j.dyepig.2023.111361.

References

[1] Kumar A, Kim D, Kumar S, Mahammed A, Churchill DG, Gross Z. Milestones in corrole chemistry: historical ligand syntheses and post-functionalization. Chem Soc Rev 2023;52:573–600.
[2] Kumar A, Yadav P, Majdoub M, Saltsman I, Fridman N, Kumar S, Kumar A, Mahammed A, Gross Z. Corroles: the hitherto elusive parent macrocycle and its metal complexes. Angew Chem Int Ed 2021;60:25097–103.
[3] Di Natale C, Gros CP, Paolesse R. Corroles at work: a small macrocycle for great applications. Chem Soc Rev 2022;51:1277–335.
[4] Alemayehu AB, Thomas KE, Einrem RF, Ghosh A. The story of 5d metallocorroles: from metal-ligand misfits to new building blocks for cancer phototherapeutics. Acc Chem Res 2021;54:3095–107.
[5] Orlowski R, Gryko D, Gryko DT. Synthesis of corroles and their heteroanalogs. Chem Rev 2017;117:3102–37.
[6] Gryko DT, Fox JP, Goldberg DP. Recent advances in the chemistry of corroles and core-modified corroles. J Porphyr Phthalocyanines 2004;8:1091–105.
[7] Senge MO, Sergeeva NN, Hale KJ. Classic highlights in porphyrin and porphyrinoid total synthesis and biosynthesis. Chem Soc Rev 2021;50:4730–89.
[8] Umasekhar B, Shetti VS, Ravikanth M. Heterocorroles: corrole analogues containing heteroatom(s) in the core or at a meso-position. RSC Adv 2018;8:21100–32.
[9] Lemon CM, Powers DC, Huynh M, Maher AG, Phillips AA, Tripet BP, Nocera DG. Ag(III)···Ag(III) Argentophilic interaction in a cofacial corrole dyad. Inorg Chem 2023;62:3–17.
[10] Soll M, Sharma VK, Khoury S, Assaraf YG, Gross Z. Corrole nanoparticles for chemotherapy of castration-resistant prostate cancer and as sonodynamic agents for pancreatic cancer treatment. J Med Chem 2023;66:766–76.
[11] Zhu ZM, Peng WY, Yang W, Ling C, Zhang H, Si LP, Liu HY. Synthesis of cobalt A2B triaryl corroles bearing methoxy or hydroxyl groups and their activity in electrocatalytic hydrogen evolution. Appl Organomet Chem 2023;37:e6932/1–6932/12.
[12] Yang W, Yang G, Li MY, Liu ZY, Liao YH, Liu HY. Photodynamic antitumor activity of Gallium(III) and Phosphorus(V) complexes of trimethoxyl A2B triaryl corrole. Bioorg Chem 2022;129:106177/1–106177/12.
[13] Lemon CM, Maher AG, Anderson BL, Bloch ED, Huynh M, McCollar AL, Nocera DG. Solvent-induced spin-state change in copper corroles. Inorg Chem 2022;61:20288–98.
[14] Osterloh WR, Desbois N, Gros CP, Kadish KM. Hypercorroles formed via the tail that wagged the dog: charge transfer interactions from innocent corroles to meso-nitrophenyl substituents. Inorg Chem 2022;61:20576–86.
[15] Kubba R, Yadav O, Maji S, Fridman N, Kumar A. Synthesis, structural characterizations, electrochemical properties and DFT calculations of highly fluorescent phosphorus(V) corroles. J Mol Struct 2022;1269:133780/1–133780/10.
[16] Sharma VK, Stark M, Fridman N, Assaraf YG, Gross Z. Doubly stimulated corrole for organelle-selective antitumor cytotoxicity. J Med Chem 2022;65:6100–15.
[17] Marinas V, Platzer B, Labella J, Caroleo F, Nardis S, Paolesse R, Guldi DM, Torres T. Controlling electronic events through rational structural design in subphthalocyanine-corrole dyads: synthesis, characterization, and photophysical properties. Chem Eur J 2022;28. e202201552/1- e202201552/11.
[18] Caroleo F, Diedenhofen G, Catini A, Di Natale C, Paolesse R, Lvova L. Phosphorous (V) corrole fluorophores for nitrite assessment in environmental and biological samples. Chemosensors 2022;10:107/1–107/12.
[19] Agresti A, Berionni BB, Pescetelli S, Catini A, Menchin F, Di Natale C, Paolesse R, Di Carlo A. Copper-based corrole as thermally stable hole transporting material for perovskite photovoltaics. Adv Funct Mater 2020;30. 20037901-2003792003790/11.
[20] Sahu K, Angeloni S, Conradie J, Villa M, Nayak M, Ghosh A, Ceroni P, Kar S. NIR-emissive, singlet-oxygen-sensitizing gold tetra(thiocyano)corroles. Dalton Trans 2022;51:13236–45.
[21] Osterloh WR, Desbois N, Quesneau V, Brandes S, Fleurat-Lessard P, Fang Y, Blondeau-Patissier V, Paolesse R, Gros CP, Kadish KM. Old dog, new tricks: innocent, five-coordinate cyanocobalt corroles. Inorg Chem 2020;59:8562–79.
[22] D'Souza F, Chitta R, Ohkubo K, Tasior M, Subbaiyan NK, Zandler ME, Rogacki MK, Gryko DT, Fukuzumi S. Corrole−fullerene dyads: formation of long-lived charge-separated states in nonpolar solvents. J Am Chem Soc 2008;130(43):14263–72.
[23] Mahammed A, Chen K, Vestfrid J, Zhao J, Gross Z. Phosphorus corrole complexes: from property tuning to applications in photocatalysis and triplet–triplet annihilation upconversion. Chem Sci 2019;10(29):7091–103.
[24] Ziegler CJ, Sabin JR, Geier GR, Nemykin VN. The first TDDFT and MCD studies of free base triarylcorroles: a closer look into solvent-dependent UV-visible absorption. Chem Commun 2012;48:4743–5.
[25] Rhoda HM, Crandall LA, Geier III GR, Ziegler CJ, Nemykin VN. Combined MCD/DFT/TDDFT study of the electronic structure of axially pyridine coordinated metallocorroles. Inorg Chem 2015;54:4652–62.
[26] Teo RD, Hwang JY, Termini J, Gross Z, Gray HB. Fighting cancer with corroles. Chem Rev 2017;117(4):2711–29.
[27] Aviv-Harel I, Gross Z. Aura of corroles. Chem Eur J 2009;15(34):8382–94.
[28] Capuano R, Pomarico G, Paolesse R, Di Natale C. Corroles-porphyrins: a teamwork for gas sensor arrays. Sensors 2015;15(4):8121–30.
[29] Gouterman M, Sayer P, Shankland E, Smith JP. Porphyrins. 41. Phosphorus mesoporphyrin and phthalocyanine. Inorg Chem 1981;20:87–92.
[30] Jjd Sacramento, Goldberg DP. Factors affecting hydrogen atom transfer reactivity of metal-oxo porphyrinoid complexes. Acc Chem Res 2018;51:2641–52.
[31] Goldberg DP. Corrolazines: new frontiers in high-valent metalloporphyrinoid stability and reactivity. Acc Chem Res 2007;40:626–34.
[32] Ramdhanie B, Zakharov LN, Rheingold AL, Goldberg DP. Synthesis, structures, and properties of a series of four-, five-, and six-coordinate cobalt(III) triazacorrole complexes: the first examples of transition metal corrolazines. Inorg Chem 2002;41:4105–7.
[33] Ramdhanie B, Stern CL, Goldberg DP. Synthesis of the first corrolazine: a new member of the porphyrinoid family. J Am Chem Soc 2001;123:9447–8.
[34] Joslin EE, Zaragoza JPT, Siegler MA, Goldberg DP. meso-N-Methylation of a porphyrinoid complex: activating the H-atom transfer capability of an inert ReV(O) corrolazine. Chem Commun 2017;53:1961–4.
[35] Joslin EE, Zaragoza JPT, Baglia RA, Siegler MA, Goldberg DP. The influence of peripheral substituent modification on PV, MnIII, and MnV(O) Corrolazines: X-ray crystallography, electrochemical and spectroscopic properties, and HAT and OAT reactivities. Inorg Chem 2016;55:8646–60.
[36] Leeladee P, Jameson GNL, Siegler MA, Kumar D, de Visser SP, Goldberg DP. Generation of a high-valent iron imido corrolazine complex and NR group transfer reactivity. Inorg Chem 2013;52:4668–82.
[37] Furuyama T, Sugiyab Y, Yoshidab T, Kobayashi N. Synthesis of meta-methoxyphenyl substituted tetraazaporphyrin and corrolazine phosphorus(V) complexes. J Porphyr Phthalocyanines 2016;20:1075–81.
[38] Kobayashi N, Yokoyama M, Muranaka A, Ceulemans A. Formation of silicon triazacorrole and tetrabenzotriazacorrole by the ring contraction of the corresponding tetraazaporphyrin ligands. Tetrahedron Lett 2004;45:1755–8.
[39] Raboui H, Lough AJ, Szawiola AM, Bender TP. Versatile synthesis of siloxy silicon tetrabenzotriazacorroles and insight into the mode of macrocycle formation. Inorg Chem 2018;57:5174–82.
[40] Zhang XF. Tetrabenzotriazacorrole: its synthesis, reactivity, physical properties, and applications. Coord Chem Rev 2015;285:52–64.
[41] Furuyama T, Sugiya Y, Kobayashi N. Synthesis of a tetrabenzotriazacorrole μ-oxo dimer and investigation of its stacking effect. Chem Commun 2014;50:4312–4.
[42] Kobayashi N, Furuya F, Yug GC, Wakita H, Yokomizo M, Ishikawa N. Synthesis and characterization of phthalocyanines with direct Si-Si linkages. Chem Eur J 2002;8:1474–84.
[43] Fujiki M, Tabei H, Isa K. New tetrapyrrolic macrocycle: α,β,γ-triazatetrabenzcorrole. J Am Chem Soc 1986;108:1532–6.
[44] Adegoke O, Nyokong T. Unsymmetrically substituted nickel triazatetra-benzcorrole and phthalocynanine complexes: conjugation to quantum dots and applications as fluorescent "turn on" sensors. J Fluorescence 2014;24:481–91.
[45] Wang SH, Mandimutsira BS, Todd R, Ramdhanie B, Fox JP, Goldberg DP. Catalytic sulfoxidation and epoxidation with a Mn(III) triazacorrole: evidence for A "third oxidant" in high-valent porphyrinoid oxidations. J Am Chem Soc 2004;126:18–9.
[46] Lu X, Zhang XF. Phosphorous tetrabenzocorrolazine from its metal-free phthalocyanine precursor: its facile synthesis, high fluorescence emission, efficient singlet oxygen formation, and promising hole transporting material. Dyes Pigments 2020;179:108421/1–108421/7.
[47] Lazovskiy DA, Skvortsov IA, Novakova V, Stuzhin PA. Phosphorus(V) tetrapyrazinocorrolazines bearing axial aryloxy groups as pH-sensitive fluorophores and photosensitizers. Dalton Trans 2022;51:5687–98.
[48] Srivishnu KS, Rajesh MN, Banerjee D, Soma VR, Giribabu L. Novel phosphorus(V) tetrabenzotriazacorroles: synthesis, characterization, optical, electrochemical, and femtosecond nonlinear optical studies. Dalton Trans 2022;51:13779–94.
[49] Raboui H, Josey DS, Jin Y, Bender TP. Initial engineering and outdoor stability assessment of "gray/black" fullerene-free organic photovoltaics based on only two

complementary absorbing materials: a tetrabenzotriazacorrole and a subphthalocyanine. ACS Omega 2020;5:25264–72.
[50] Raboui H, Thibau ES, Josey DS, Lu ZH, Bender TP. Oxy phosphorus tetrabenzotriazacorrole: firming up the chemical structure and identifying organic photovoltaic functionality to leverage its unique dual absorbance. J Mater Chem 2017;5:10978–85.
[51] Zhang XF, Rong Y. Silicon tetrabenzotriazacorrole and silicon phthalocyanine: synthesis, photophysics and singlet oxygen generation. J Photochem Photobiol, A 2011;222:141–5.
[52] Mkhize C, Britton J, Mack J, Nyokong T. Optical limiting and singlet oxygen generation properties of phosphorus triazatetrabenzcorroles. J Porphyr Phthalocyanines 2015;19:192–204.
[53] Liu J, Zhao Y, Zhao F, Zhang F, Song X, Chau FT. Study on phosphorus(III) complex of tetrabenzotriazacorrole: a novel phthalocyanine-like photosensitizer. J Photochem Photobiol, A 1996;99:115–9.
[54] Majeed SA, Ghazal B, Nevonen DE, Nemykin VN, Makhseed S. Spectroscopic and TDDFT studies on the charge-transfer properties of metallated Octa(carbazolyl) phthalocyanines. Dyes Pigments 2019;170:107593/1–107593/13.
[55] Majeed SA, Ghazal B, Nevonen DE, Goff PC, Blank DA, Nemykin VN, Makhseed S. Evaluation of the intramolecular charge-transfer properties in solvatochromic and electrochromic zinc octa(carbazolyl)phthalocyanines. Inorg Chem 2017;56(19): 11640–53.
[56] Li J, Subramanian LR, Hanack M. Studies on phosphorus phthalocyanines and triazatetrabenzcorroles. Eur J Org Chem 1998:2759–67. 1998.
[57] Breusova MO, Pushkarev VE, Tomilova LG. Synthesis of alkyl-substituted phosphorus phthalocyanines and triazatetrabenzocorroles. Russ Chem Bull 2007; 56:1456–60.
[58] Fox JP, Goldberg DP. Octalkoxy-substituted phosphorus(V) triazatetrabenzcorroles via ring contraction of phthalocyanine precursors. Inorg Chem 2003;42:8181–91.
[59] Ghosh A, Ravikanth M. Synthesis, structure, spectroscopic, and electrochemical properties of highly fluorescent phosphorus(V)-meso-Triarylcorroles. Chem Eur J 2012;18:6386–96.
[60] Chatterjee T, Lee WZ, Ravikanth M. Stabilization of hexa-coordinated P(V) corroles by axial silyloxy groups. Dalton Trans 2016;45:7815–22.
[61] Ghosh A, Lee WZ, Synthesis Ravikanth M. Structure and properties of a five-coordinate oxophosphorus(V) meso-triphenylcorrole. Eur J Inorg Chem 2012: 4231–9. 2012.
[62] Lee W, Zhan X, Palma J, Vestfrid J, Gross Z, Churchill DG. Minding our P-block and Q-bands: paving inroads into main group corrole research to help instil broader potential. Chem Commun 2021;57:4605–41.
[63] Gao D, Azarias C, D'Aleo A, Giorgi M, Siri O, Balaban TS, Jacquemin D, Canard G. Synthesis and characterization of ruffled phosphorus meso-ester corroles. Eur J Inorg Chem 2017:780–8. 2017.
[64] Liu J, Zhang F, Zhao F, Tang Y, Song X, Yao G. Complexation of phosphorus(III) with a novel tetrapyrrolic phthalocyanine-like macrocyclic compound. J Photochem Photobiol, A 1995;91:99–104.
[65] Zhang XF, Huang J, Zhao H, Zheng X, Zhu J. Photophysical properties of nonperipherally and peripherally substituted triazatetrabenzcorrole phosphorous dihydroxy and singlet oxygen generation. J Photochem Photobiol, A 2010;215: 96–102.
[66] Antunes EM, Nyokong T. Synthesis and photophysical behavior of axially substituted phthalocyanine, tetrabenzotriazaporphyrin, and triazatetrabenzcorrole phosphorous complexes. J Porphyr Phthalocyanines 2009;13:153–60.
[67] Zhang XF, Chang Y, Peng Y, Zhang F. Substituted phosphorous triazatetrabenzocorroles: correlation between structure and excited state properties. Aust J Chem 2009;62:434–40.
[68] Huang L, Zhao P, Li Z, Zhang F, Tung CH. Photophysical properties of sulfonated dihydroxy phosphorus(V) tetrabenzotriazacorrole. J Phys Chem A 2008;112: 4165–9.
[69] Furuyama T, Sugiya Y, Kobayashi N. Synthesis of a tetrabenzotriazacorrole μ-oxo dimer and investigation of its stacking effect. Chem Commun 2014;50:4312–4.
[70] Shi M, Tian J, Mkhize C, Kubheka G, Zhou J, Mack J, Nyokong T, Shen Z. Synthesis, characterization and photodynamic therapy properties of an octa-4-tert-butylphenoxy-substituted phosphorus(V) triazatetrabenzcorrole. J Porphyr Phthalocyanines 2014;18:698–707.
[71] Kadish KM, Ou Z, Adamian VA, Guilard R, Gros CP, Erben C, Will S, Vogel E. Corroles with group 15 Ions. 2. Synthesis and characterization of octaethylcorroles containing a phosphorus central atom. Inorg Chem 2000;39:5675–82.
[72] Paolesse R, Boschi T, Licoccia S, Khoury RG, Smith KM. Phosphorus complex of corrole. Chem Commun 1998:1119–20.
[73] Akiba KY, Nadano R, Satoh W, Yamamoto Y, Nagase S, Ou Z, Tan X, Kadish KM. Synthesis, structure, electrochemistry, and spectroelectrochemistry of hypervalent phosphorus(V) octaethylporphyrins and theoretical analysis of the nature of the PO bond in P(OEP)(CH2CH3)(O). Inorg Chem 2001;40:5553–67.
[74] Ghidinelli S, Abbate S, Mazzeo G, Paolesse R, Pomarico G, Longh G. MCD and MCPL characterization of luminescent Si(IV) and P(V) tritolylcorroles: the role of coordination number. ACS Omega 2021;6:26659–71.
[75] Mack J, Bunya M, Lansky D, Goldberg DP, Kobayashi N. The MCD spectroscopy of corrolazines and triazatetrabenzocorroles. Heterocycles 2008;76:1369–80.
[76] Waluk J, Michl J. Perimeter model and magnetic circular dichroism of porphyrin analogs. J Org Chem 1991;56:2729–35.
[77] Michl J. Magnetic circular dichroism of cyclic .pi.-electron systems. 2. Algebraic solution of the perimeter model for the B terms of sys-tems with a (4N + 2)-electron [n]annulene perimeter. J Am Chem Soc 1978;100:6812–8.
[78] Belosludov RV, Nevonen DE, Rhoda HM, Sabin JR, Nemykin VN. Simultaneous prediction of the energies of Qx and Qy bands and intramolecular charge-transfer transitions in benzoannulated and non-peripherally substituted metal-free phthalocyanines and their analogues: No standard TDDFT silver bullet yet. J Phys Chem A 2019;123:132–52.
[79] Nemykin VN, Kobayashi N, Chernii VY, Belsky VK. Mossbauer, crystallographic, and density functional theoretical investigation of the electronic structure of bis-ligated low-spin iron(II) phthalocyanines. Eur J Inorg Chem 2001;3:733–43.
[80] Martynov AG, Mack J, May AK, Nyokong T, Gorbunova YG, Tsivadze AY. Methodological survey of simplified TD-DFT methods for fast and accurate interpretation of UV-Vis-NIR spectra of phthalocyanines. ACS Omega 2019;4: 7265–84.
[81] Nemykin VN, Basu P. Comparative theoretical investigation of the vertical excitation energies and the electronic structure of $[Mo^{V}OCl_4]^-$: influence of basis set and geometry. Inorg Chem 2003;42:4046–56.
[82] Zerner M, Gouterman M. Porphyrins. IV. Extended Hueckel calculations on transition metal complexes. Theor Chim Acta 1966;4:44–63.
[83] Gouterman M. Spectra of porphyrins. J Mol Spectrosc 1961;6:138–63.
[84] Seybold PG, Gouterman M. Porphyrins. J Mol Spectrosc 1969;31:1–13.
[85] Armarego WLF, Perrin DD. Purification of laboratory chemicals. fourth ed. Reed Elsevier; 1997.
[86] Frisch MJ, Trucks GW, Schlegel HB, Scuseria GE, Robb MA, Cheeseman JR, Scalmani G, Barone V, Petersson GA, Nakatsuji H, Li X, Caricato M, Marenich AV, Bloino J, Janesko BG, Gomperts R, Mennucci B, Hratchian HP, Ortiz JV, Izmaylov AF, Sonnenberg JL, Williams, Ding F, Lipparini F, Egidi F, Goings J, Peng B, Petrone A, Henderson T, Ranasinghe D, Zakrzewski VG, Gao J, Rega N, Zheng G, Liang W, Hada M, Ehara M, Toyota K, Fukuda R, Hasegawa J, Ishida M, Nakajima T, Honda Y, Kitao O, Nakai H, Vreven T, Throssell K, Montgomery Jr JA, Peralta JE, Ogliaro F, Bearpark MJ, Heyd JJ, Brothers EN, Kudin KN, Staroverov VN, Keith TA, Kobayashi R, Normand J, Raghavachari K, Rendell AP, Burant JC, Iyengar SS, Tomasi J, Cossi M, Millam JM, Klene M, Adamo C, Cammi R, Ochterski JW, Martin RL, Morokuma K, Farkas O, Foresman JB, Fox DJ. Gaussian 16. Wallingford, CT: Rev. C.01; 2016.
[87] Becke AD. Density-functional thermochemistry. III. The role of exact exchange. J Chem Phys 1993;98(7):5648–52.
[88] Lee C, Yang W, Parr RG. Development of the Colle-Salvetti correlation-energy formula into a functional of the electron density. Phys Rev B 1988;37(2):785–9.
[89] Heyd J, Scuseria GE. Efficient hybrid density functional calculations in solids: assessment of the Heyd–Scuseria–Ernzerhof screened Coulomb hybrid functional. J Chem Phys 2004;121(3):1187–92.
[90] Heyd J, Scuseria GE. Assessment and validation of a screened Coulomb hybrid density functional. J Chem Phys 2004;120(16):7274–80.
[91] Schaefer HF, editor. Modern theoretical chemistry, vol. 3. New York, NY: Plenum; 1976.
[92] Tomasi J, Mennucci B, Cammi R. Quantum mechanical continuum solvation models. Chem Rev 2005;105(8):2999–3093.
[93] Tenderholt AL. QMForge. Stanford, CA: Stanford University; 2011., Version 2.1. https://qmforge.net/.